

# Chapter 5

## Screening for Perylene Diimide Acceptors

In this chapter, we present a screening for acceptor molecules with perylene diimide groups (Fig. 5.1) for application in organic solar cells. In the opening section 5.1, we introduce a collection of polyene diimide derivatives and present structural design strategies concerning the impact on the performance of organic solar cells (e.g. the power conversion efficiency, PCE). We develop an *in silico* screening and apply it to 13 derivatives (Fig. 5.1). For instance, we compare the stability of structural conformations, their chirality, and the resulting optoelectronic properties as well as the charge transfer properties on the basis of aggregation patterns. First, we present the compounds individually (Sec. 5.2 to 5.7) and compare them afterwards (Sec. 5.8). (See Comp. Details 2.3) Parts of the sections 5.3 for PPD [321] and 5.4 for HDI [395] have already been published.

### 5.1 Introduction

Perylene diamide derivatives are non-fullerene acceptor molecules for application in bulk heterojunction organic solar cells [47]. In the last decades, perylene bisimide dyes (PBI, derived from perylene-3,4:9,10-bis(dicarboximide) or often also abbreviated as PDI from perylene-3,4:9,10-tetracarboxylic acid diimide [396] were used due to a multitude of favourable properties found in fundamental studies [62, 63, 311, 320, 321, 395, 396] (see Fig. 5.1).

Unlike conventional fullerene-based derivatives like PC<sub>61</sub>BM [306] or PC<sub>71</sub>BM [307], polyene diamide derivatives offer:

- (i) Higher absorption in the visible red spectral energy regime, in individual cases up to a strong visible-NIR light-harvesting capability in line with high molar absorption coefficients,
- (ii) Easy access for chemical modifications,
- (iii) Enhanced possibilities for tuning optical and electronic properties, via the optical bandgap due to designed shifts in frontier orbital energy levels,
- (iv) Good properties in BHJ-OSC devices, as reliable long term stability, supporting high open-circuit voltage ( $V_{OC}$ ) and short-circuit current densities ( $J_{SC}$ ) [14],
- (v) Higher power conversion efficiencies (PCE) in devices.

A sizable number of different perylene bisimide (PBI) derivatives have been synthesised in the past [47]. They link the favourable properties of an extended aromatic conjugated  $\pi$ -system, facilitating high absorbance with the electron-withdrawing characteristic of the imide motive promoting molecular electron affinity. An imide group is a functional group consisting of two acyl groups bound to a nitrogen atom (Fig. 5.1). As polyene diamide derivatives can bear several of these functional groups, they possess high electron affinities and give rise to high electron mobilities (Sec. 5.2).

Favourable synthetic strategies for novel electron acceptors include the fusion of several PDI subunits [310,311,396] or the incorporation of heteroatoms to influence the conjugated  $\pi$ -system [312,318,319]. The most common modifications of PDI are alternations of the aliphatic side chains at the imide position and functionalisation or ring fusion at the  $\alpha$ -position or in the bay region [47,397]. These non-planar perylene structures are introduced in order to prevent the molecules from forming large crystalline aggregated domains [314]. Unfortunately, the twists in the acceptor molecules are suspected of impeding charge transport [315]. It is reported that a smaller extend of intramolecular twists can enhance the PCE in systems, where several side groups are aligned around a central aromatic core motive [313].

The DIPBI molecule [62] is made up of two linked PDI units and possesses a slightly twisted, non-planar geometry (Fig. 5.1,2). DIPBI builds  $\pi$ -stacks [64] that facilitate electron transport inside the domains (see Sec. 3.1.1). As charge carriers may be trapped inside isolated DIPBI domains, they do not reach the electrodes and recombine, which reduces the PCE. In P3HT:DIPBI solar cells, a PCE of 3.62% is reported [63].

In order to overcome this drawback, PPDI was designed, which is made up of two PDI units that are linked in a head-tail-fashion and the PDI planes are predominantly oriented orthogonal to each other (Fig. 5.1,3). Therefore, PPDI is more flexible than DIPBI, and it can participate with the first arm in one  $\pi$ -stack and with the second in another, which enhances the interconnectivity between adjacent stacks. PPDI is the electron donor in PBDT-TS1:PPDI solar cells, which give rise to a PCE about 5.40% [311] (see Sec. 4.2).

TPH [320] consists of three PDI unites that are oriented around a central benzene core and form a twisted propeller conformation (Sec. 5.2). They build three-dimensional networks for charge transport, with a PCE of 8.28% in PDBT-T1:TPH in BHJ-OSCs. The introduction of Se atoms enhances the formation of networks in TPH-Se (Fig. 5.1,4) via Se-O interactions, which lead to an enhanced PCE of 9.28% in PDBT-T1:TPH-Se. Similar diastereoisomers with *N*-annulated triperylene hexaimides at the bay-position yield a lower PCE of 8.11% [398]. It is reported for a similar system PDBT-T1:SdiPBI-Se [312] that the inclusion of selenium (Se) atoms in the bay-region of PBI leads to an enhanced performance of 8.4% in the PCE. This design strategy [321] is extended to twisted propeller molecules containing five blades in pentaperylenen decaimides (PPD) and the selenium-annulated form PPD-Se (Fig. 5.1,5) (see Sec. 5.3).

Nonetheless, most fabricated BHJ-OSCs are based on fullerene derivatives and a conjugated polymer and achieve a PCE over 11% [399], due to their high electron transport properties in three-dimensional networks. PCEs of over 10% have been reported for organic solar cells based on non-fullerene acceptor molecules and polymer donors as well, e.g. up to 13.1% [400] in single-junction devices, and tandem devices 13.8% [401]. The PCEs in these systems outperform the best fullerene-based OSCs.

An alternative route for rylene-based non-fullerene acceptors are A-D-A semiconductors, which possess a push-pull structure that combine electron-withdrawing units (A) with a central electron-donating moiety (D), which can be linked by a conjugated spacer unit.

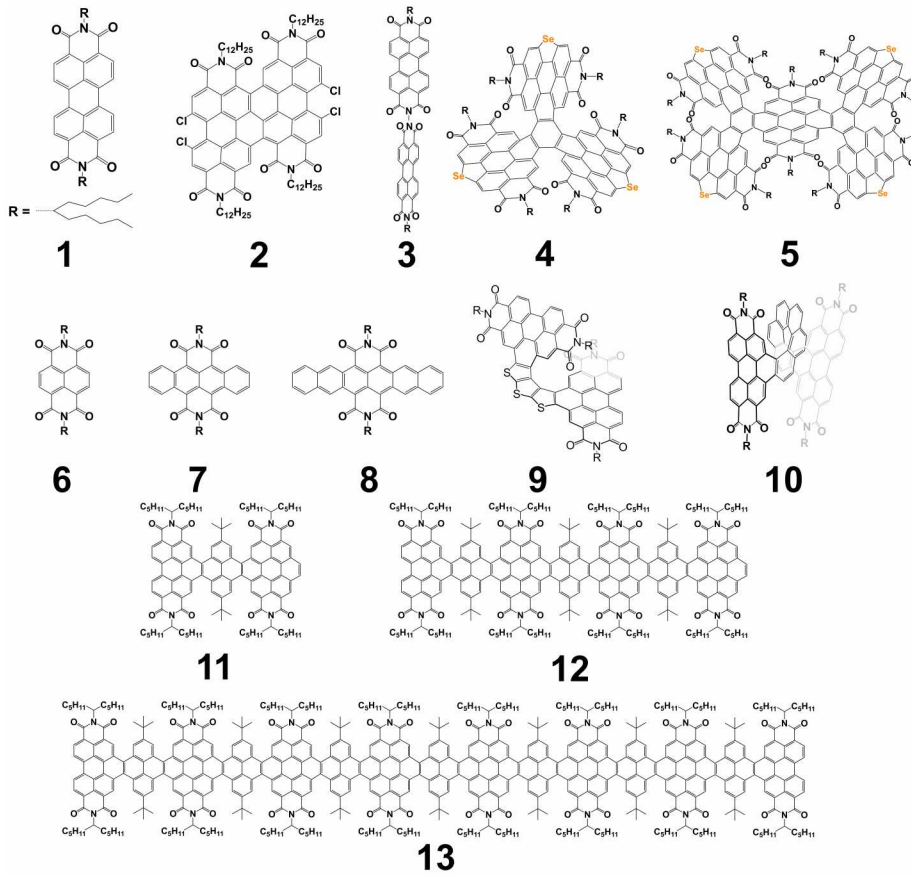


Figure 5.1: Chemical structures for non-fullerene acceptor molecules discussed in this thesis. 1) perylene bisimides (PBI) [62] 2) tetrachlorinated diperylene bisimide (DIPBI) [62,63] 3) a nonplanar dimeric PBI derivative (PPDI) [311] 4) selenium-annulated triperylene hexaimides (TPH-Se) [320] 5) selenium-annulated pentaperylenen decaimides (PPD-Se) [321] 6) naphthalene diimide (NDI) [395] 7) tetracene diimide (TDI) [395] 8) hexacene diimide (HDI) [395] 9) *M*-PDTT1 10) *M*-PHHP-AS 11) laddered nanoribbons: PDI2-Pyr1 12) PDI4-Pyr3 13) PDI8-Pyr7.

Two examples of this class are ITIC with a PCE of 11.77% [402] and Y6 exhibits a high PCE of 15.7% in PM6:Y6 [394]. Even the 18% PCE limit has already been exceeded with the D18:Y6 system, so there is great potential to increase the OSC efficiency of future devices [16,32]. Three-dimensional graphene nanostructures with a PDI motive achieve a remarkable PCE of 18% as electron-extracting layers in perovskite solar cells [403].

Suitable candidates for charge transport in organic semiconductors are also small molecules as naphthalene diimides (NDI) [404, 405], tetracene diimides (TDI) [406] and hexacene diimide (HDI) [395] (Fig. 5.1,6,7,8) (see Sec. 5.4).

An alternative route to PDI-based acceptor molecules is the strategy to use ring-fusion to extend the delocalisation of an excess charge, tailoring co-planarity of a molecule and enhancing the packing order [62,309,407]. Several types of spacer units have been applied successfully to link PDI [317], e.g. furan, thiophene, selenophene, benzene [316]. The ring-fusion leads to an enhanced intramolecular coupling, which lifts the LUMO and thereby causes a blue-shift in the absorption spectrum [316]. Hence, a promising strategy for higher PCEs is the elongation of a thiophene-based spacer to tailor the intramolecular twist.

For instance, this method is applied in *M*-PDTTI (Fig. 5.1,9) (see Sec. 5.5). Furthermore, there are chiral molecules similar to PHHP-AS (Fig. 5.1,10) with a (clockwise) *P* and (anticlockwise) *M* alignment of two PDI units that are connected by a naphthalene spacers in the literature [408] (see Sec. 5.6).

The linking of PDI units can give rise to distinct conformation motives as helical, wagging and a mixed zig-zag relative PDI orientation [409]. One can combine this strategy using pyrene subunit as a spacer [410]. In this spirit, the laddered nanoribbons, e.g. twistacens [411] and the class of *PDI<sub>n</sub>-Pyr(*n* - 1)* as PDI2-Pyr1, PDI4-Pyr3, and PDI8-Pyr7 (Fig. 5.1,11,12,13) are appealing candidates for efficient electron acceptor molecules in OSCs (see Sec. 5.7).

The goal of the following sections (Sec. 5.2 to 5.7) is to characterise the presented series of acceptor molecules concerning structural and spectral properties. Especially, we compare different aggregation patterns and charge transfer properties, e.g.  $\lambda_{\text{in}}^{\text{h/e}}$ ,  $|J_{\text{AB}}^{\text{h/e}}$ , and  $k_{\text{AB}}^{\text{h/e}}$ . The approach based on dimer configurations is used as screening for favourable intermolecular alignment patterns for efficient charge transport in the amorphous phase. This yields the perspective to deduce hints for design strategies for novel acceptor compounds that are beneficial for application in future BHJ-OSCs (Sec. 5.8).

## 5.2 Triperylene Hexaimides (TPH / TPH-Se)

Rylene-based acceptors and their derivatives offer a promising route to efficient acceptor molecules in organic solar cells [308]. Triperylene hexaimides (TPH) and selenium-annulated triperylene hexaimides (TPH-Se) [320] consist of three PBI units attached to a central benzene core. They form twisted, three-bladed propeller molecules due to a strong steric hindrance (see Fig. 5.1,4). TPH forms four stereoisomers and two pairs of corresponding enantiomers. Both molecules exhibit a broad absorption in the range 400-600 nm. TPH features two absorption maxima at 366 nm and 516 nm.

In organic field-effect transistors, the maximal reported electron mobility for TPH is  $\mu_e = 0.028 \text{ cm}^2/\text{Vs}$  in single crystal and a slightly higher mobility  $\mu_e = 0.032 \text{ cm}^2/\text{Vs}$  for TPH-Se [320]. In a PDBT-T1:TPH blend film, the electron mobility is reported  $\mu_e = 1.5 \times 10^{-3} \text{ cm}^2/\text{Vs}$  and the hole mobility  $\mu_h = 1.0 \times 10^{-3} \text{ cm}^2/\text{Vs}$ . The values for mobilities in the TPH-Se are slightly higher  $\mu_e = 2.2 \times 10^{-3} \text{ cm}^2/\text{Vs}$  and  $\mu_h = 1.7 \times 10^{-3} \text{ cm}^2/\text{Vs}$ .

The incorporation of chalcogen atoms into rylene-imide based organic solar cells is regarded as a strategy to control intermolecular interactions, molecular orientations in bulk and at the donor-acceptor interface [319]. Comparing the features of PBDB-TF:TPH solar cells to PBDB-TF:TPH-Se, one finds that TPH-Se maintains face-on orientation and exhibits smaller domain sizes, due to a higher ordered packing motive, which is assigned to Van der Waals interactions between the selenium atoms in the acceptor and oxygen atoms in the backbone of the donor. As a consequence, this interaction is regarded to detail an enhanced  $\pi$ -orbital overlap and  $\pi$ -stacking, which facilitates charge transfer and reduces the polaron binding energy at the donor-acceptor interface. The Se atoms cause a higher distortion in the propeller molecule and the facilitation for arrangements in three-dimensional networks is attributed to Se-O interactions [320]. The Se-annulated triperylene hexaimides yields an enhanced PCE 9.63% compared to 8.65% in TPH [319].

We find an internal reorganization energy  $\lambda_h^{\text{in}} = 0.133 \text{ eV}$  for hole transfer between pairs of TPH molecules and  $\lambda_e^{\text{in}} = 0.161 \text{ eV}$  for electrons (B3LYP-D3(BJ)/6-31G\*). In comparison to TPH, we obtain only a slight increase in TPH-Se  $\lambda_h^{\text{in}} = 0.138 \text{ eV}$  and  $\lambda_e^{\text{in}} = 0.169 \text{ eV}$ .

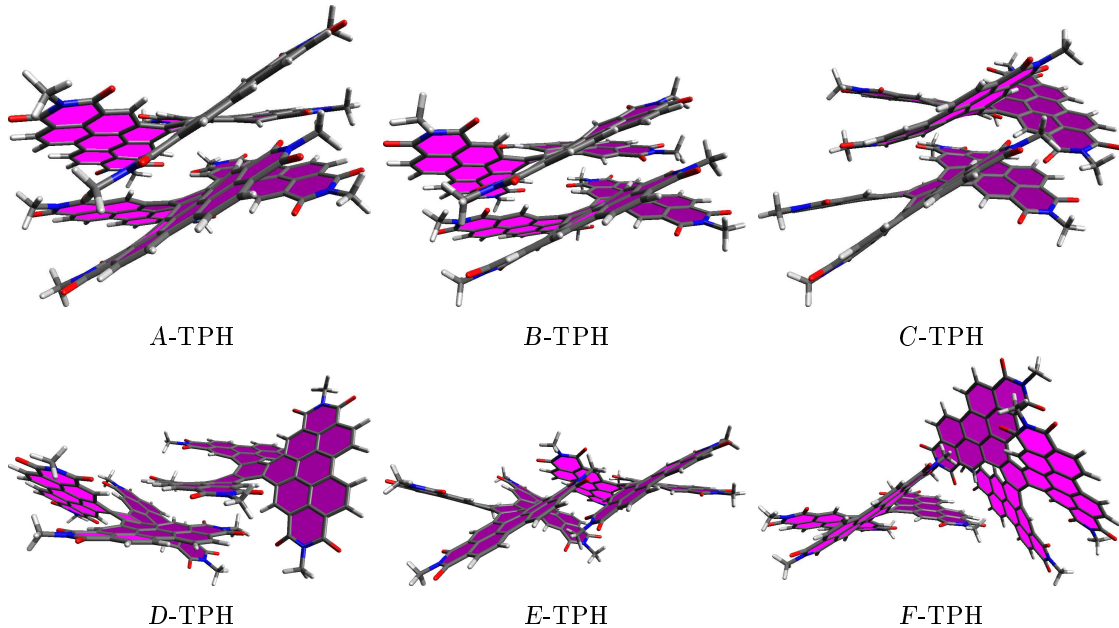


Figure 5.2: Optimised ground state geometries of stacking aggregates for TPH dimers on B3LYP-D3(BJ)/6-31G\* level of theory. The different dimer structures are labelled with *A* to *F*. The PDI propeller blades are marked in violet.

The dimers for TPH yield different aggregation motives (Fig. 5.2). The lowest total energy is found for dimer *A*-TPH, where the PDI blades are aligned to form a screw-like  $\pi$ -stack with a contact zone for all blades. The dimer configuration *B*-TPH is similar but yields a small lateral shift. Also, *C*-TPH is a  $\pi$ -stacking aggregate, where the central ring of one TPH is located parallel to the centre of a neighbouring PDI unit. One finds a lateral stack in dimer *D*-TPH, with one PDI blade on top of two nearby PDI units. The laterally aligned dimer *E*-TPH and the T-stack in *F*-TPH yield high total energies.

We find high charge transfer properties for the TPH dimer configurations *A*, *B* and *E*, whereas *C*, *D* and *F* yield lower values (Tab. 5.1). For instance, *B*-TPH exhibits  $|J_{AB}^h| = 6.46 \times 10^{-2}$  eV and  $|J_{AB}^e| = 2.32 \times 10^{-2}$  eV, which enable pronounced Marcus charge transfer rates  $k_{AB}^h = 1.88 \times 10^{13}$  s<sup>-1</sup> and  $k_{AB}^e = 1.01 \times 10^{13}$  s<sup>-1</sup>. Both  $\pi$ -stack configurations *A*-TPH and *B*-TPH yield elevated rates at the order  $1.0 \times 10^{13}$  s<sup>-1</sup>. Besides, *E*-TPH yields  $|J_{AB}^{h/e}| \approx 1 \times 10^{-2}$  eV and an enhanced  $k_{AB}^e = 1.05 \times 10^{13}$  s<sup>-1</sup>. In contrast, the TPH dimers *C*, *D* and *F* only yield  $|J_{AB}^{h/e}|$  at the order of  $\approx 1.0 \times 10^{-3}$  eV that result in reduced  $k_{AB}$  between  $10^9$  s<sup>-1</sup> and  $10^{12}$  s<sup>-1</sup>.

The TPH-Se dimers exhibit similar packing motives as the TPH dimers (Fig. 5.3). Dimer sites with a lateral Se-O interaction are only found in configuration *F*-TPH-Se, with a distance of  $d_{Se-O} = 3.15$  Å and  $d_{Se-O} = 3.02$  Å. However, we do not find enhanced Marcus charge transfer rate in this configuration and particularly no significant increase in this *F*-TPH-Se configuration compared to *F*-TPH. The lateral alignment in *E*-TPH-Se is mostly favourable for electron transfer, which is indicated by a high  $|J_{AB}^e| = 5.91 \times 10^{-2}$  eV and a high transfer rate  $k_{AB}^e = 1.33 \times 10^{14}$  s<sup>-1</sup>. Hence, *E*-TPH and *E*-TPH-Se yield beneficial charge transfer values. The *D*-TPH-Se configuration is ambiguous as it yields a high  $k_{AB}^h$  and a small  $k_{AB}^e$  owing to a difference of about two orders of magnitude in the charge transfer integrals  $|J_{AB}^{h/e}|$ . The analysis of Se-annulated TPH dimer configurations corroborates the finding for beneficial configurations *A*, *B* and *E* compared to *C* and *F*.

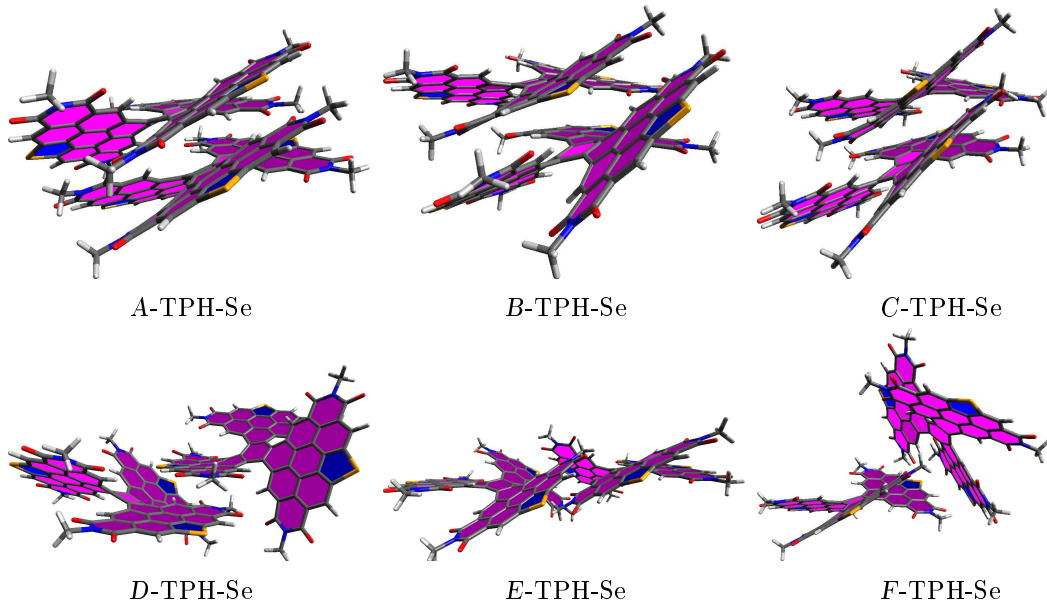


Figure 5.3: Optimised ground state geometries of stacking aggregates for TPH-Se dimers on B3LYP-D3(BJ)/6-31G\* level of theory. The different dimer structures are labelled with A to F. The PDI propeller blades are marked in violet.

On average TPH-Se exhibits higher electron transfer rates  $\bar{k}_{AB}^e = (2.24 \pm 5.43) \times 10^{13} \text{ s}^{-1}$  than TPH  $\bar{k}_{AB}^e = (4.42 \pm 4.32) \times 10^{12} \text{ s}^{-1}$ . This trend matches the enhanced trend of the electron mobility in PDBT-T1:TPH-Se compared to PDBT-T1:TPH. Moreover, the slightly reduced hole transport in PDBT-T1:TPH-Se compared to electron transport is reflected in the reduced average hole rate  $\bar{k}_{AB}^h = (7.09 \pm 5.27) \times 10^{11} \text{ s}^{-1}$  in TPH-Se. In contrast, the higher  $\bar{k}_{AB}^h = (7.06 \pm 11.1) \times 10^{12} \text{ s}^{-1}$  in TPH compared to TPH-Se does not meet the expected experimental trend.

Table 5.1: Marcus charge transfer rates between optimised dimer structures for TPH and TPH-Se for hole transport  $k_{AB}^h$  and electron transport  $k_{AB}^e$  on B3LYP-D3(BJ)/6-31G\* level of theory. Furthermore, the relative energies with respect to the most stable aggregation and the charge transfer integral  $|J_{AB}^{h/e}|$  based on DIPRO calculations are presented.

dimer conformation	$E_{\text{rel}} / \text{eV}$	$ J_{AB}^h  / \text{eV}$	$k_{AB}^h / \text{s}^{-1}$	$ J_{AB}^e  / \text{eV}$	$k_{AB}^e / \text{s}^{-1}$
A-TPH	0.000	8.07E-2	2.94E+13	1.61E-2	4.85E+12
B-TPH	0.001	6.46E-2	1.88E+13	2.32E-2	1.01E+13
C-TPH	1.101	7.65E-3	1.60E+11	4.68E-3	5.19E+11
D-TPH	2.776	5.22E-3	2.05E+10	2.21E-3	1.69E+11
E-TPH	2.928	1.84E-2	1.50E+11	1.67E-2	1.05E+13
F-TPH	3.151	3.89E-3	6.07E+09	6.13E-3	1.43E+12
A-TPH-Se	0.000	1.56E-2	1.04E+12	5.53E-3	5.17E+11
B-TPH-Se	1.856	1.88E-2	8.42E+11	5.56E-3	6.94E+11
C-TPH-Se	1.885	1.63E-2	6.33E+11	2.06E-3	9.51E+10
D-TPH-Se	3.708	5.25E-2	1.47E+12	4.80E-4	7.87E+09
E-TPH-Se	4.111	2.38E-2	1.49E+11	5.94E-2	1.33E+14
F-TPH-Se	4.324	1.42E-2	1.14E+11	3.09E-4	3.23E+09

### 5.3 Pentaperylene Decaimides (PPD / PPD-Se)

The synthesis of nanographenes with large conjugated  $\pi$ -systems has made significant progress in recent years, and the development of novel compounds varying in size, shape and substitution pattern is of great interest for the design of optoelectronic devices [308,412,413]. One approach to strongly distorted nanographenes is the use of helicene moieties with a twisted  $\pi$ -conjugated system in a dendrimer synthesis strategy, as applied in hexapole helicene (HH) with a sixfold [5]helicene substructures [414].

A representative of the group of nanographene imides is pentaperylenen decaimides (PPD) [321], which contains sixfold [5]helicenes around two benzene cores equipped with imide groups (Fig. 5.1,5). PPD features a central perylene diimides (PDI) unit and four laterally, adjacent PDI wings. Variations in the relative orientation of the PDI subunits result in 28 possible stereoisomers, which are grouped into 14 enantiomer pairs. They are classified into symmetry groups, with six conformers having C<sub>1</sub> symmetry, six having C<sub>2</sub> symmetry and two having D<sub>2</sub> symmetry (Fig. 5.4). The same categorisation applies to the corresponding 14 enantiomers (See Table S2 in Ref. [321] for comparison).

However, only one pair of enantiomers is obtained selectively in chiral high-pressure liquid chromatography (HPLC). The enantiomers with D<sub>2</sub> symmetry are labelled (P, P, P, P, P, P) and (M, M, M, M, M, M), where P denotes the plus (clockwise) orientation and M represents the minus (counter-clockwise) orientation of the adjacent PDI wings in the bay region of the central benzene ring.

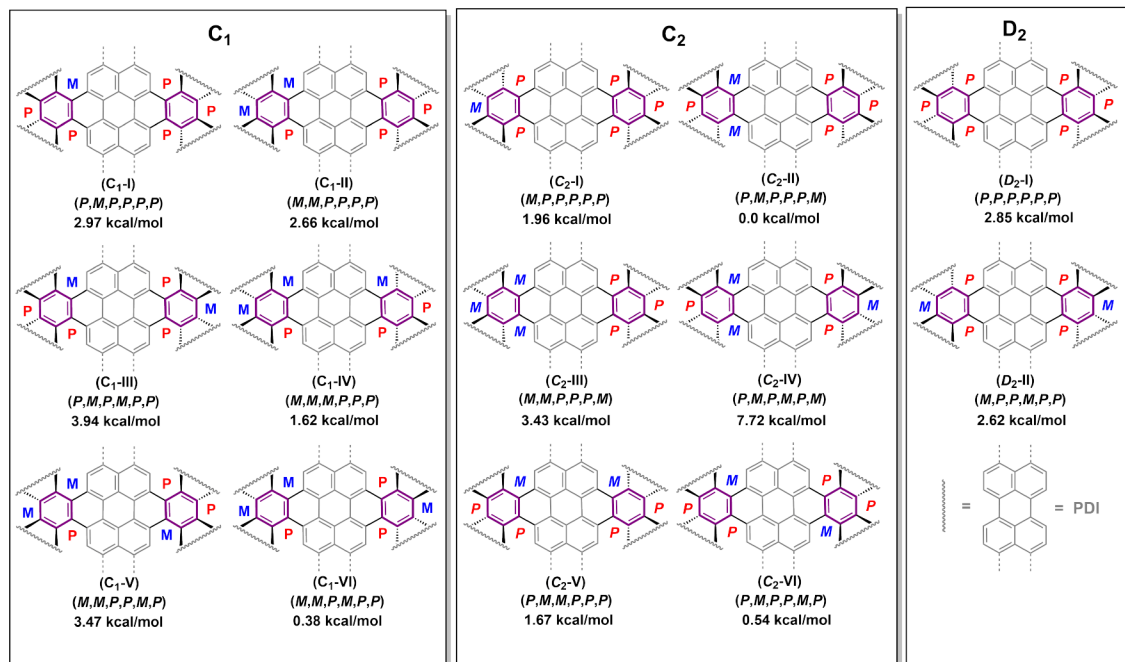


Figure 5.4: Stereoisomers of nanographene imides featuring sixfold [5]helicenes around two benzene cores (PPD). The structures are arranged according to their symmetry groups C<sub>1</sub>, C<sub>2</sub> and D<sub>2</sub>. The labels P (plus, clockwise) and M (minus, counterclockwise) denote the orientation of each two neighbouring PDI wings in the bay region of the central benzene rings. The relative free energies  $\Delta G_{\text{rel}}$  are determined at the optimised ground state S<sub>0</sub> geometries, including the zero-point vibration energies and the thermal free energies at  $T = 300$  K on B3LYP-D3(BJ)/6-31G\* level of theory in chloroform solution [321].

Both enantiomers can be distinguished in experimental circular dichromism (CD) and assigned to the conformers (*P,P,P,P,P,P*) and (*M,M,M,M,M,M*) by electronic circular dichroism spectra (ECD) (Fig. 5.5). The mirror-imaged CD spectra have a  $\Delta\epsilon$  value in the range of  $\Delta\epsilon = \pm 200 \text{ M}^{-1}\text{cm}^{-1}$  and exhibit intricate alternating patterns, that are in satisfactory agreement with the evaluated transitions in ECD spectra. PPD shows three Cotton effects in the visible part of the spectrum. In contrast, HH provides the characteristic Cotton effects in ultraviolet spectral range [414]. Furthermore, PPD has an anisotropic dissymmetry *g*-factor of  $g \approx 2 \times 10^{-3}$  (see Eq. 95), which is comparable to that of HH.

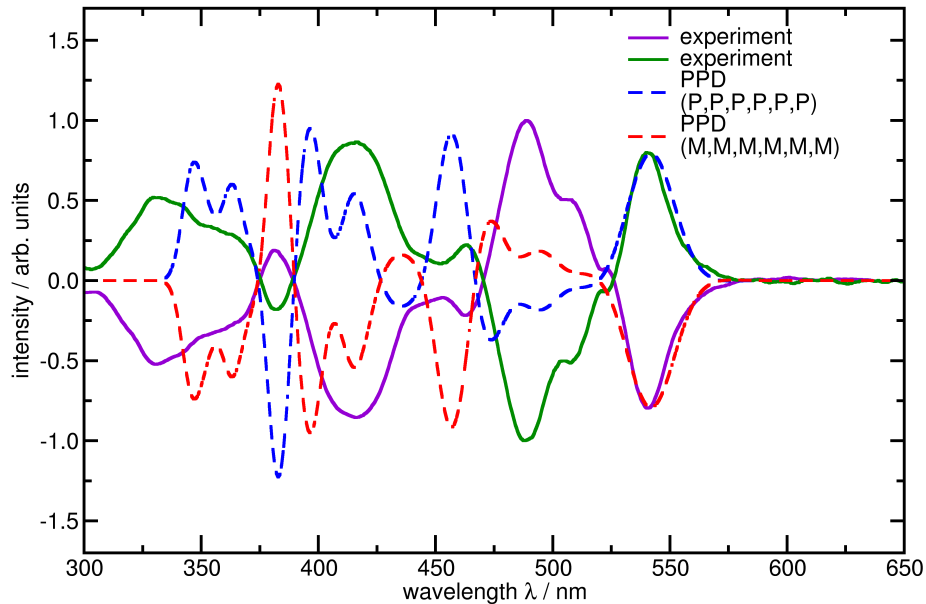


Figure 5.5: Electronic circular dichroism spectra for chiral PPD enantiomers in the (*P,P,P,P,P,P*) conformation and (*M,M,M,M,M,M*) conformation at the optimised  $S_0$  structure at PBE0-D3(BJ)/6-31G\* level in the gas phase.

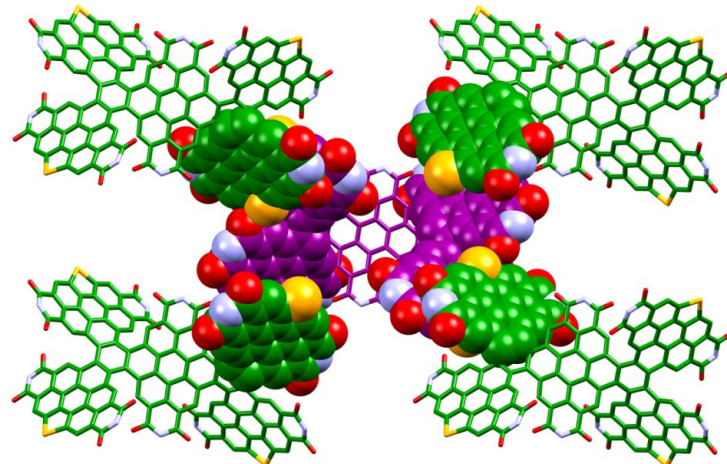


Figure 5.6: Single-crystal X-ray structure and stacked packing pattern of PPD-Se in the crystal reveals the intermolecular  $\pi$ - $\pi$  interactions between the (green) enantiomer (*P,P,P,P,P,P*) and the (purple) enantiomer (*M,M,M,M,M,M*) [321].

X-ray diffraction analysis unravels the 'four-bladed propeller' conformation in the PPD-Se single-crystal structure. The chiral conformations ( $P, P, P, P, P, P$ ) (Fig. 5.6) and ( $M, M, M, M, M, M$ ) are stacked to form a compact three-dimensional network. The PDI units of neighbouring conformers ( $P, P, P, P, P, P$ ) and ( $M, M, M, M, M, M$ ) form  $\pi$ -stacks with slipped intermolecular  $\pi$ - $\pi$  interactions. This type of molecular junctions facilitates charge transport and leads to a network of conductive charge-transport channels.

The conformations are relatively stable and do not undergo any transition to another conformational structure, even if the sample is heated in diphenyl ether at 200°C for six hours. The theoretically determined activation energy for flipping two outer PDI units past each other is 54.85 kcal/mol, while 59.13 kcal/mol is required to pass an outer PDI unit past the central PDI unit (Fig. 5.7). The free energies ( $\Delta G$  values) for all PPD and PPD-Se stereoisomers are presented in the Supporting Information in Table S2 [321].

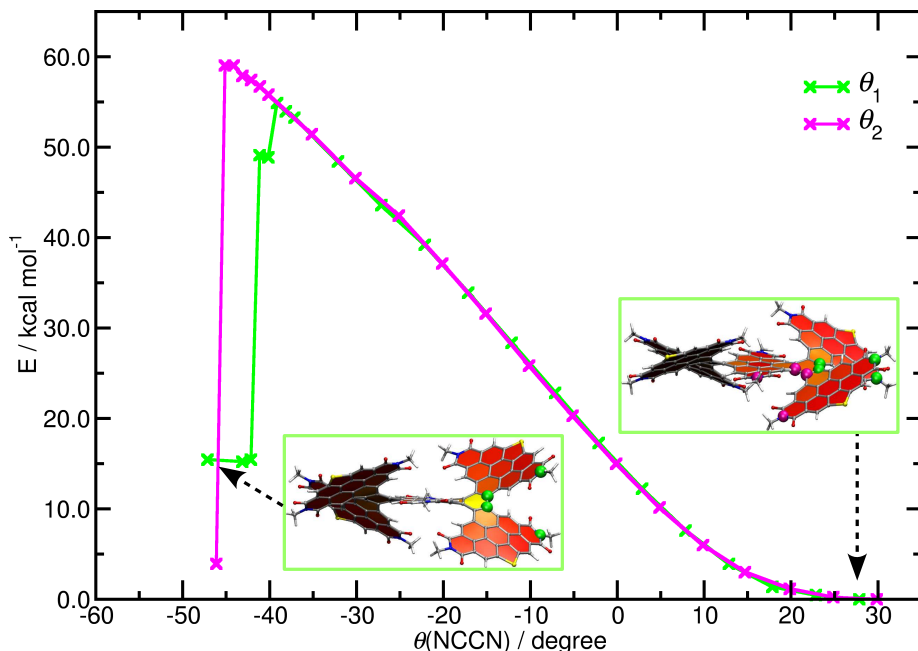


Figure 5.7: The energy barriers of PPD-Se are depicted for the conformational changes from the ( $P, P, P, P, P, P$ ) conformation to ( $P, M, P, P, P, P$ ) with associated energy  $E(\theta_1)$  and to conformation ( $M, P, P, P, P, P$ ) with the energy barrier  $E(\theta_2)$  as a function of the dihedral angles  $\theta_1$  and  $\theta_2$  based on constrained geometry optimisations at B3LYP-D3(BJ)/6-31G\* level of theory in chloroform solution. The barrier heights  $E_{\max}(\theta_1) = 54.85$  kcal/mol and  $E_{\max}(\theta_2) = 59.13$  kcal/mol are too high to be overcome by thermal activation. The dihedral angle is decreased going from PPD-Se conformation ( $P, P, P, P, P, P$ ) (on the right-hand side) to the ( $P, M, P, P, P, P$ ) and ( $M, P, P, P, P, P$ ) conformations (left-hand side) [321]. The dihedral angles  $\theta_1$  (green atoms) and  $\theta_2$  (magenta atoms) are defined visually in the molecular structures: ( $P, P, P, P, P, P$ ) (right) and ( $P, M, P, P, P, P$ ) (left).

The TDDFT absorption spectra are consistent with the UV-Vis absorption as PPD and PPD-Se exhibit high absorption in the spectral range between 300 nm and 600 nm with a maximum at 603 nm in the low energy range (Fig. 5.8). PPD possesses two main absorption bands with a high molar extinction coefficient  $\varepsilon = 1.72 \times 10^5 \text{ M}^{-1} \text{ cm}^{-1}$  at 376 nm and about  $\varepsilon = 1.5 \times 10^5 \text{ M}^{-1} \text{ cm}^{-1}$  in the second band, which is in the range from 483 nm to 535 nm.

The absorption spectrum of PPD-Se exhibits the same characteristics as PPD. However, it is red-shifted by 26-36 nm compared to PPD. In accordance with TDDFT calculations at the theoretical level of B3LYP-D3(BJ)/6-31G\*, the first absorption peak of PPD at 603 nm is dominated by a transition from the ground state  $S_0$  to the first excited singlet state  $S_1$ , which arises essentially due to HOMO to LUMO+2 excitation. Transitions from  $S_0$  to  $S_5$ ,  $S_7$  and  $S_8$  determine the absorption band in the range from 483 nm to 535 nm. A high oscillator strength  $f = 1.19$  is found for state  $S_{49}$ , which dominates the absorption band at 376 nm. In contrast to PPD, the low-energy excitation for PPD-Se is a HOMO to LUMO excitation. The second absorption peak is assigned to the two states  $S_4$  and  $S_6$ . The band at 412 nm is dominated by the  $S_{58}$  state, which has an oscillator strength of  $f = 0.86$ . Comparing the absorbance of PPD and PPD-Se to the absorbance of the three-bladed perylene propellers TPH and TPH-Se shows an increase of about 1.1-1.9 times.

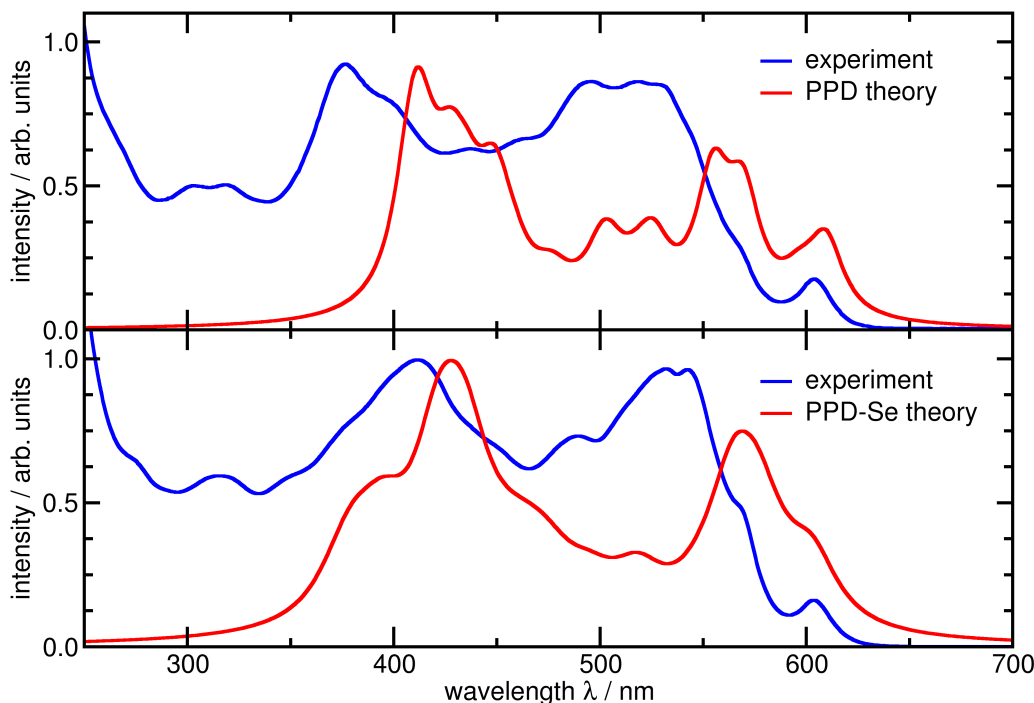


Figure 5.8: UV-Vis absorption spectra of PPD (upper panel) and PPD-Se (lower panel) in  $\text{CHCl}_3$  solution at room temperature and TDDFT absorption spectra for PPD and PPD-Se in conformation ( $P, P, P, P, P, P$ ) on B3LYP-D3(BJ)/6-31G\* level.

PPD and PPD-Se show fluorescence emission with a maximum intensity at 617 nm and 601 nm, respectively (Fig. 5.9). Also the fluorescence quantum yield of 24% for PPD is higher than 15% for TPH. The improved fluorescence and absorption features for PPD compared to TPH suggest that the incorporation of more PDI units into nanographene imides structures is a suitable design strategy for novel compounds. The quenching of the fluorescence quantum yield with the incorporation of Se atoms in PPD-Se to 6% can be attributed to a heavy-atom effect [415].

The DFT-based LUMO levels in the solultion are -3.26 eV for PPD and PPD-Se and the HOMO levels are -5.70 eV for PPD and -5.73 eV for PPD-Se, respectively. This capacity makes PPD and PPD-Se suitable candidates as non-fullerene electron acceptor material in organic solar cells.

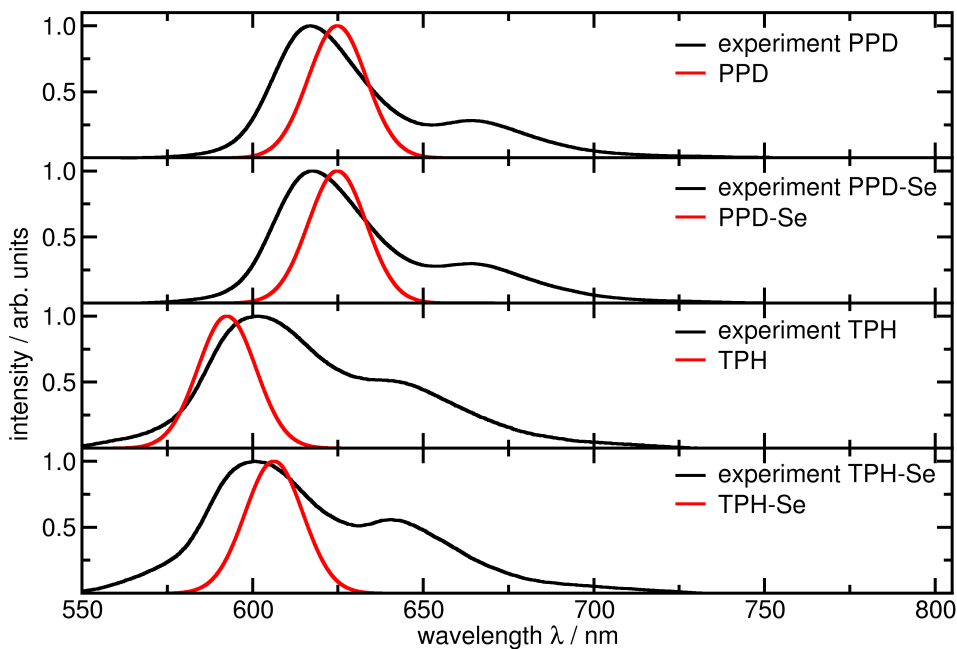


Figure 5.9: Experimental fluorescence spectra of PPD, PPD-Se, TPH and TPH-Se in  $\text{CHCl}_3$  solution at room temperature and theoretical spectra on PBE0-D3(BJ)/6-31G\* level of theory.

We compare six optimised ground state geometries for PPD dimers in Fig. 5.10. The monomers show a face-on orientation in both structures *A*-PPD and *B*-PPD, where all five PDI blades are as close as possible. This is also reflected in the small  $d_{\text{MMA}} = 3.75 \text{ \AA}$  and  $d_{\text{MMA}} = 3.69 \text{ \AA}$ . One monomer exhibits a slight lateral shift in *B*-PPD concerning *A*-PPD configuration. Each monomer participates with three PDI blades in the  $\pi$ -stacking aggregation patterns in both *C*-PPD and *D*-PPD. The distances  $d_{\text{MMA}} = 4.41 \text{ \AA}$  and  $d_{\text{MMA}} = 4.06 \text{ \AA}$  therefore increase. The PPD monomers are rotated against each other by an angle of  $\vartheta \approx 41^\circ$ . Also *C*-PPD and *D*-PPD yield a small lateral shift. A further reduction of the interaction space is found in *E*-PPD, where only two PDI blades of each monomer are close to each other and  $d_{\text{MMA}} = 6.30 \text{ \AA}$ . *F*-PPD forms a T-stack. In total,  $d_{\text{MMA}}$  quantifies the increasing intermolecular distance from *A* to *F*.

In *A*-PPD-Se, we find five PDI blades close to the neighbouring monomer, which is similar to *A*-PPD (Fig. 5.11). All presented PPD-Se configurations *A* to *F* are similar to the corresponding PPD structures with one exception *B*-PPD-Se. The *B*-PPD-Se structure exhibits only four PDI-PDI interaction sites.

The PPD-Se dimer pairs for *G-I* are extracts of the crystal structure from X-ray diffraction analysis (Fig. 5.11). The illustrations focus on the intermolecular junctions between PDI blades. The PPD-Se structures *A* to *F*, which represent the amorphous phase, are more densely packed than in the crystal structures *G-I* with  $d_{\text{MMA}} > 10 \text{ \AA}$ .

*A*-PPD and *B*-PPD yield the highest hole transfer rates  $k_{\text{AB}}^{\text{h}}$  at about  $1.31 \times 10^{12} \text{ s}^{-1}$  and  $2.22 \times 10^{12} \text{ s}^{-1}$ , respectively. The PPD conformations *D*, *E*, and *F*, exhibit lower Marcus rates  $k_{\text{AB}}^{\text{h}}$  at the order of  $1.0 \times 10^{10} \text{ s}^{-1}$ . In turn, *D*-PPD has the maximum electron transfer rate  $k_{\text{AB}}^{\text{e}} = 1.62 \times 10^{14} \text{ s}^{-1}$  as a consequence of a high  $|J_{\text{AB}}^{\text{e}}| = 5.25 \times 10^{-3} \text{ eV}$ . *A*-PPD and *B*-PPD show high electron transfer rates  $k_{\text{AB}}^{\text{e}}$  at the order of  $1.0 \times 10^{13} \text{ s}^{-1}$  as well. Even though *D*-PPD is structurally similar to *C*-PPD, the charge transfer rates differ clearly.

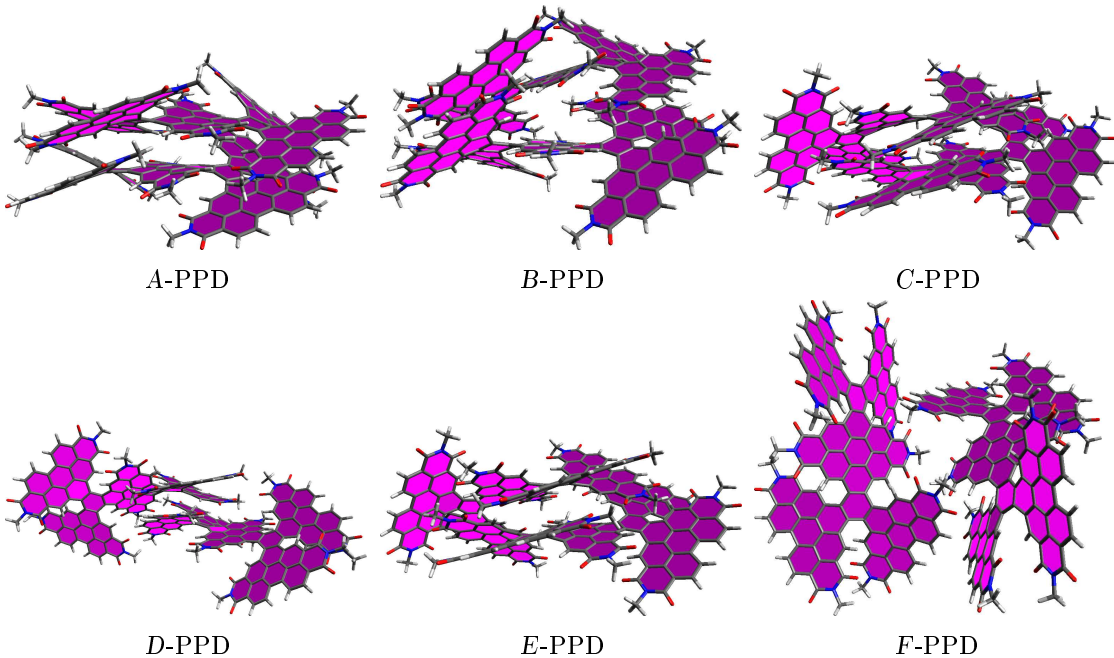


Figure 5.10: Optimised ground state geometries of stacking aggregates for PPD dimers on B3LYP-D3(BJ)/6-31G\* level of theory. The different dimer structures are labelled with A to F. The PDI propeller blades are marked in violet.

In general, the PPD conformers yield higher average electron transfer rates  $\bar{k}_{AB}^e = (4.02 \pm 6.21) \times 10^{13} \text{ s}^{-1}$  than hole transfer rates  $\bar{k}_{AB}^h = (4.77 \pm 9.09) \times 10^{11} \text{ s}^{-1}$ . This trend is also marginally reflected in the averaged charge transfer integrals as  $|\bar{J}_{AB}^e| = (2.01 \pm 1.92) \times 10^{-2} \text{ eV}$  slightly exceeds  $|\bar{J}_{AB}^h| = (1.17 \pm 0.66) \times 10^{-2} \text{ eV}$ .

We find the highest hole transfer rate  $k_{AB}^h = 5.39 \times 10^{12} \text{ s}^{-1}$  in A-PPD-Se. It is exceeded by the highest electron transfer rate  $k_{AB}^e = 1.20 \times 10^{14} \text{ s}^{-1}$  in D-PPD-Se, which is similar to D-PPD. B-PPD-Se and E-PPD-Se yield low rates.

All three junctions G, H and I in the PPD-Se crystal structure exhibit only one  $\pi$ -stacking site. Hence, the charge transfer integrals  $|\bar{J}_{AB}^e| = (2.44 \pm 0.89) \times 10^{-3} \text{ eV}$  and  $|\bar{J}_{AB}^h| = (6.16 \pm 0.48) \times 10^{-3} \text{ eV}$  are lower than those found for the dimers representing the amorphous phase (A to F). The average transfer rates  $\bar{k}_{AB}^e = (2.91 \pm 1.98) \times 10^{11} \text{ s}^{-1}$  and  $\bar{k}_{AB}^h = (4.01 \pm 0.69) \times 10^{11} \text{ s}^{-1}$  are at the same order of magnitude. Despite, they are significantly smaller than in the configurations A-PPD-Se to F-PPD-Se. As only one single PDI blade participates at  $\pi$ -stacking between neighbouring PPD-Se in the crystal structures G, H and I, the charge transfer rates are not as high as those for the optimised dimer structures A-PPD-Se to F-PPD-Se. The ladder exhibit more than one intermolecular interaction site.

Although, we find a reduction in the intermolecular PDI-PDI contact space from A to F, which is quantified by the tendency for increasing distance  $d_{MMA}$ , a trend for decreasing charge transfer integrals and rates is only partially reflected in the data. This finding underlines the sensitivity of  $|J_{AB}|$  and  $k_{AB}$  on the underlying dimer structure. As a result, the investigation rebuts the presumption that a simple increment in the number of PDI-PDI  $\pi$ -stacking motives consequently result in higher intermolecular charge transfer properties.

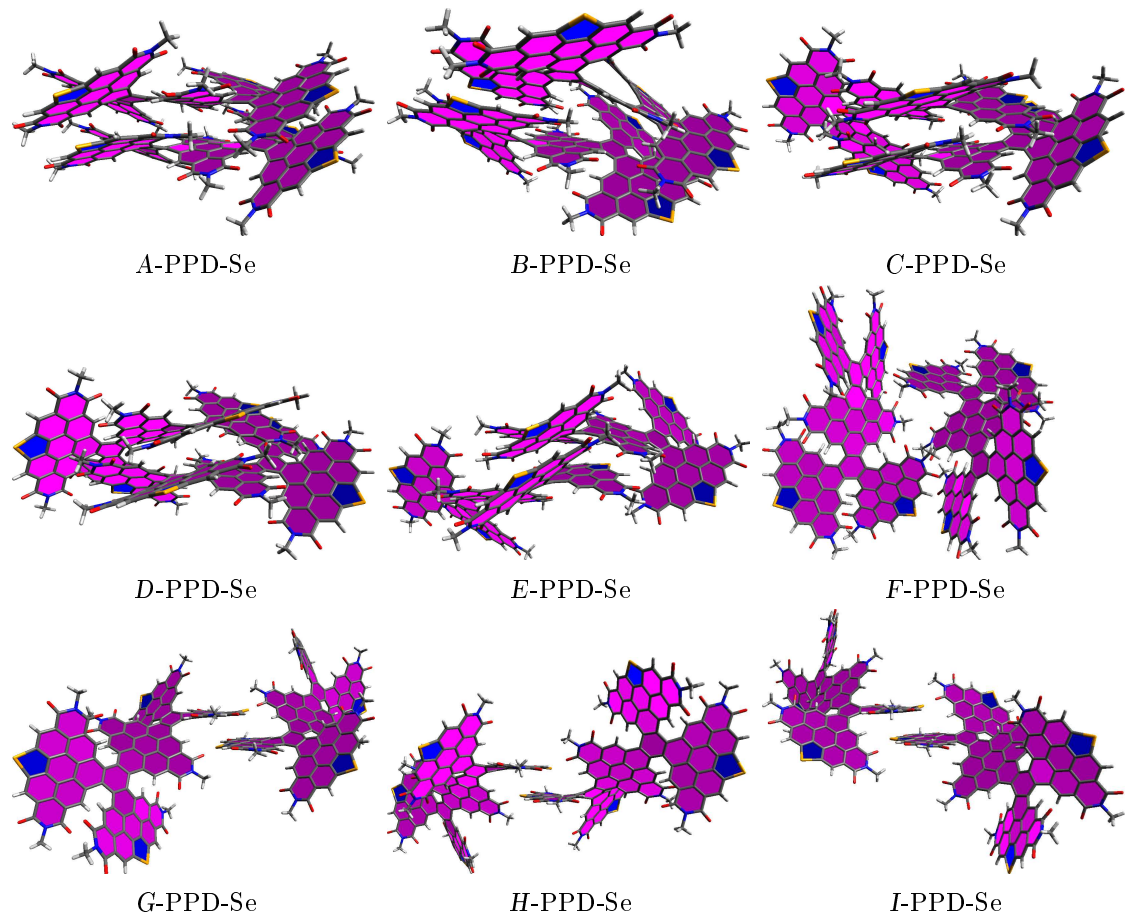


Figure 5.11: Optimised ground state geometries of stacking aggregates for PPD-Se dimers on B3LYP-D3(BJ)/6-31G\* level of theory. The different dimer structures are labelled with *A* to *I*. The dimer pairs *G* to *I* are extracted from the crystal structure based on X-ray diffraction analysis [321]. The PDI propeller blades are marked in violet.

Table 5.2: Marcus charge transfer rates between optimised dimer structures for PPH and PPH-Se for hole transfer  $k_{AB}^h$  and for electron transfer  $k_{AB}^e$  on B3LYP-D3(BJ)/6-31G\* level of theory. Furthermore, the relative energies  $E_{\text{rel}}$  with respect to the most stable aggregation, the mean minimal appearing distance  $d_{\text{MMA}}$  (Eq. 274) and the charge transfer integral  $|J_{AB}^{h/e}|$  based on DIPRO calculations are presented.

conformation	$E_{\text{rel}} / \text{eV}$	$d_{\text{MMA}} / \text{\AA}$	$ J_{AB}^h  / \text{eV}$	$k_{AB}^h / \text{s}^{-1}$	$ J_{AB}^e  / \text{eV}$	$k_{AB}^e / \text{s}^{-1}$
A-PPD	0.000	3.75	1.58E-2	1.31E+12	2.68E-2	3.83E+13
B-PPD	0.013	3.68	2.06E-2	2.22E+12	2.52E-2	3.41E+13
C-PPD	0.946	4.41	1.47E-2	4.77E+11	4.56E-3	1.23E+12
D-PPD	0.993	4.06	2.51E-3	1.46E+10	5.25E-2	1.62E+14
E-PPD	2.713	6.30	6.97E-3	1.29E+10	1.11E-2	5.16E+12
F-PPD	3.307	7.68	9.38E-3	2.53E+10	2.31E-4	2.28E+09
A-PPD-Se	0.000	3.66	3.21E-2	5.39E+12	2.80E-2	4.52E+13
B-PPD-Se	0.960	4.16	3.63E-3	3.87E+10	1.12E-3	7.78E+10
C-PPD-Se	1.386	4.15	1.43E-2	4.96E+11	2.90E-2	5.19E+13
D-PPD-Se	1.416	4.23	2.60E-2	1.51E+12	4.42E-2	1.20E+14
E-PPD-Se	3.344	5.97	2.35E-3	1.61E+09	7.95E-3	2.49E+12
F-PPD-Se	5.524	7.69	1.04E-2	3.08E+10	1.27E-2	6.24E+12
G-PPD-Se crystal	0.000	10.16	6.71E-3	4.80E+11	1.57E-3	1.09E+11
H-PPD-Se crystal	0.188	10.17	5.82E-3	3.62E+11	3.36E-3	5.01E+11
I-PPD-Se crystal	0.375	10.80	5.95E-3	3.60E+11	2.39E-3	2.60E+11

## 5.4 Hexacene Diimides (HDI)

Since the early days of organic semiconductors, acenes have played an important role in organic electronic devices [416]. In particular, pentacene is one of the widely studied acenes, both experimentally and theoretically, due to its optical properties, high conductivity and charge carrier mobility in both crystalline and amorphous structures [211, 417, 418].

The extension of the conjugated  $\pi$ -system of acenes to lower the bandwidth is an appealing pathway. Extended acenes suffer from two significant disadvantages, one is lower solubility, and the other is high reactivity, which reduces their potential applications. Therefore, the synthesis of acene imides fuels the hope to overcome some drawbacks as the incorporation of the strong electron-withdrawing imide group into the acene backbone gives rise to a smaller bandgap, good optical and electron transport properties, and even the application as ambipolar semiconductors in organic field-effect transistors (OFETs) is possible [395].

Here, the focus is on three distinct acene imides (Fig. 5.1,6,7,8), namely hexacene diimides (HDIs) [395], tetracene diimides (TDIs) [406] and naphthalene diimides (NDIs) [404, 405]. Apart from a good solubility in organic solvents, HDI also offers high thermal stability and resistance to modifications of substance properties upon light and oxygen exposure under ambient conditions. The outstanding features of HDI are remarkable high, ambipolar transport properties  $\mu^e = 2.17 \text{ cm}^2/\text{Vs}$  and  $\mu^h = 0.30 \text{ cm}^2/\text{Vs}$  in OFET devices.

In the following calculations, we substitute the aliphatic side chains by methyl groups to reduce computational efforts without missing valuable insight, which is in line with the experimental findings that HDIs with three different branched alkyl side chains exhibit almost the same absorption properties (SI Figure S2 [395]). Furthermore, this result is an indicator that aggregation processes of multiple HDI molecules are absent in a dilute  $\text{CHCl}_3$  solution.

DFT calculations on PBE0-D3(BJ)/6-31G\* level suggest that the HDI backbone in hexacene is planar, whereas the dicarboximide rings are inclined by an angle of  $\vartheta \approx 9^\circ$ . This is because the carboxide group and the hydrogen have a steric hindrance, which can also be found in TDI single-crystal structure [406]. The extended hexacene backbone and comparatively planar molecular geometry give HDI utile intermolecular  $\pi$ -stacking abilities.

The experimental absorption spectra in the ultraviolet-visible near-infrared (UV-Vis-NIR) spectral range and theoretical TDDFT absorption spectra for HDI, TDI and NDI are compared in Fig. 5.12. HDI possesses three major absorption bands in the wavelength range 300 nm to 1100 nm in a diluted  $\text{CHCl}_3$  solution. Three absorption maxima appear in the HDI spectrum at 335 nm, 498 nm, and 950 nm.

The adsorption bands can be attributed to electronic transitions using TDDFT eigenvectors (see SI Fig. S5 and Tab. S3-S5 [395]). The lowest energy peak emerges from the lowest excited singlet state  $S_1$  with a 98.3% HOMO-LUMO contribution. The medium level energy peak at 498 nm arises from the  $S_3$  state with prevalent contributions from a HOMO-2 to LUMO transition with a 92.5% weight. The energy peak with maximum absorption at 335 nm is attributed to the excited states  $S_{14}$  and  $S_{16}$ . The  $S_{14}$  state predominantly comprises transitions from the HOMO-1 to the LUMO+1 with a contribution of 54.2% and from the HOMO to the LUMO+2 with a contribution of 36.0%, whereas the  $S_{16}$  possesses a weight of 92.1% from the HOMO to LUMO+3 transition.

The absorption spectra for NDI and TDI are also presented for comparison (Fig. 5.12). The absorption maximum of HDI in the low-energy range is considerably red-shifted with respect to TDI and NDI by 195 nm and 568 nm as a result of the increased elongation of the conjugated  $\pi$ -system of the backbone. In analogy to HDI, the  $S_1$  state in NDI and TDI is also given by a pure HOMO-LUMO transition and the oscillator strength increases when reducing the system size.

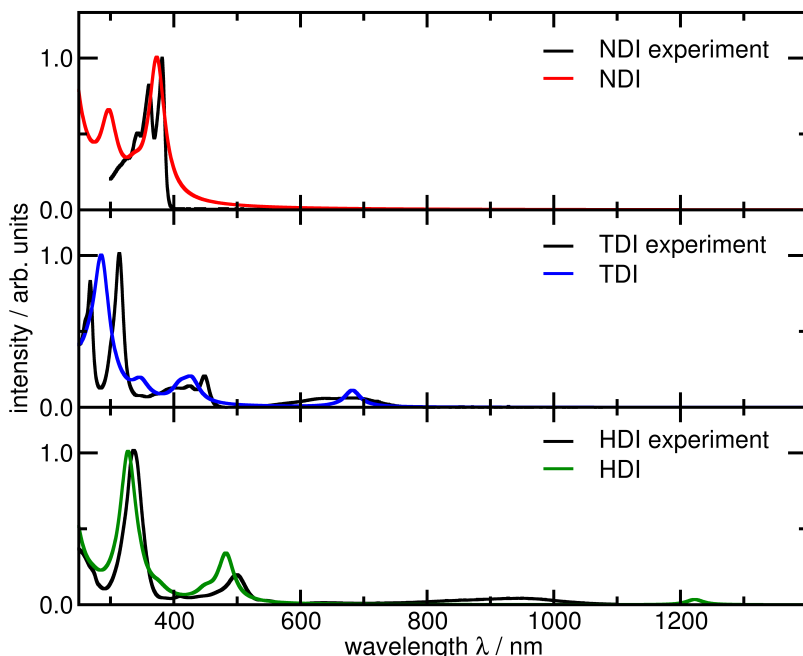


Figure 5.12: UV-Vis-NIR absorption spectra and TDDFT absorption spectra for NDI, TDI, HDI monomers at the optimised  $S_0$  geometry at PBE0-D3(BJ)/6-31G\* level in  $\text{CHCl}_3$  solution.

The bandgap decreases with increasing system size, e.g.  $E_g = 3.97$  eV in NDI, 2.38 eV in TDI, and 1.54 eV in HDI. This trend of increasing expansion in a delocalised  $\pi$ -system, which leads to a decrease in the bandgap energy  $E_g$ , is also consistent with the findings in a 2D model for a particle in a box [419, 420]. Besides, the overall trend in the frontier orbital energies  $E_{\text{LUMO}} = -3.35$  eV (NDI),  $-3.71$  eV (TDI) and  $-3.96$  eV (HDI) and  $E_{\text{HOMO}} = -7.32$  eV,  $-6.09$  eV and  $-5.50$  eV is consistent with the trends of experimental results in cyclic voltammetry [395]. These findings emphasise the increasing impact of the imides' electron-withdrawing abilities with an extension of the delocalised  $\pi$ -system.

**Aggregates of Hexacene Diimides** Geometry optimisations in the electronic ground state  $S_0$  for different HDI dimer conformations result in three distinct HDI dimer structures, labelled (A, B, C). The dimer structures belong to local minima on the potential energy surface of the ground state and are shown in Fig. 5.13.

The HDI dimers form  $\pi$ -stacking aggregates with a different overlap in the delocalised  $\pi$ -system of neighbouring HDI monomers. The A-HDI dimer conformation has the lowest total energy, followed by B-HDI with a higher relative energy of  $\Delta E_{\text{rel}} = 0.324$  eV and C-HDI with  $\Delta E_{\text{rel}} = 0.646$  eV. The binding energy  $\Delta E_B$  is evaluated with respect to the total energy of two isolated HDI monomers ( $\Delta E_B = E_{\text{dimer}} - 2E_{\text{monomer}}$ ). It tops out at  $\Delta E_B = -2.07$  eV for dimer A-HDI, and the absolute value decreases to  $-1.75$  eV for B-HDI and  $-1.43$  eV for C-HDI, respectively.

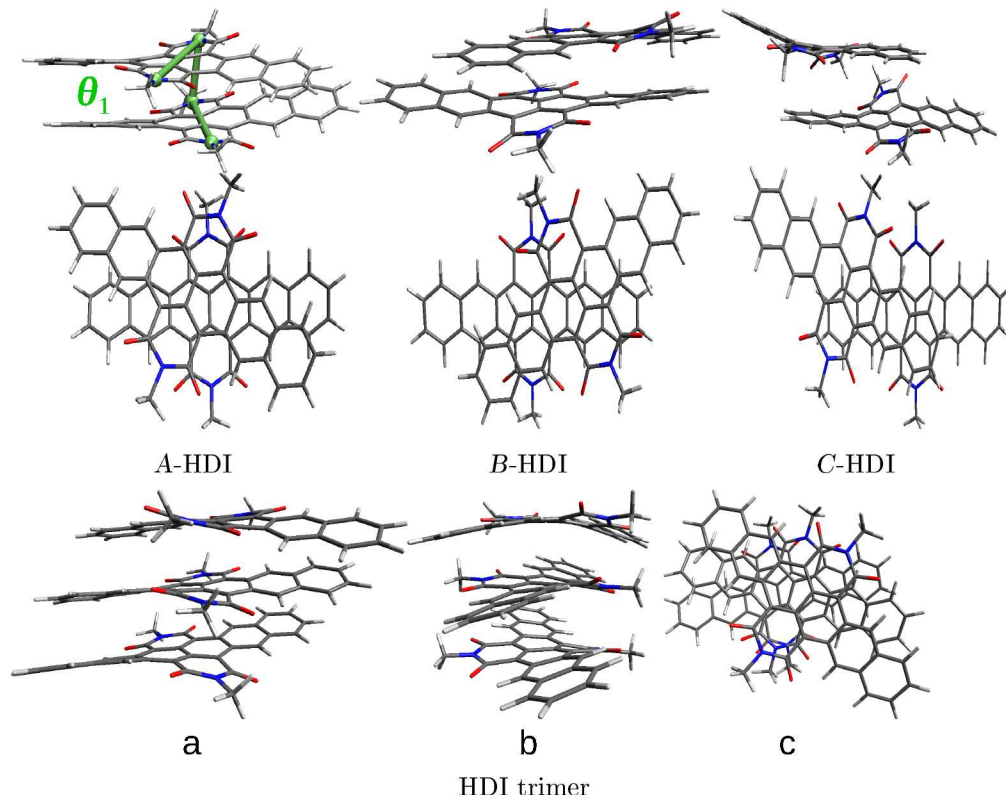


Figure 5.13: HDI dimer structures in configurations A, B, C and ordered with respect to their relative total  $S_0$  energy differences  $\Delta E_{\text{rel}}$  to configuration A (upper panel). HDI trimer structure a) front view b) side view c) top view (lower panel). All structures are optimised at ground state  $S_0$  on PBE0-D3(BJ)/6-31G\* level in  $\text{CHCl}_3$  solution.

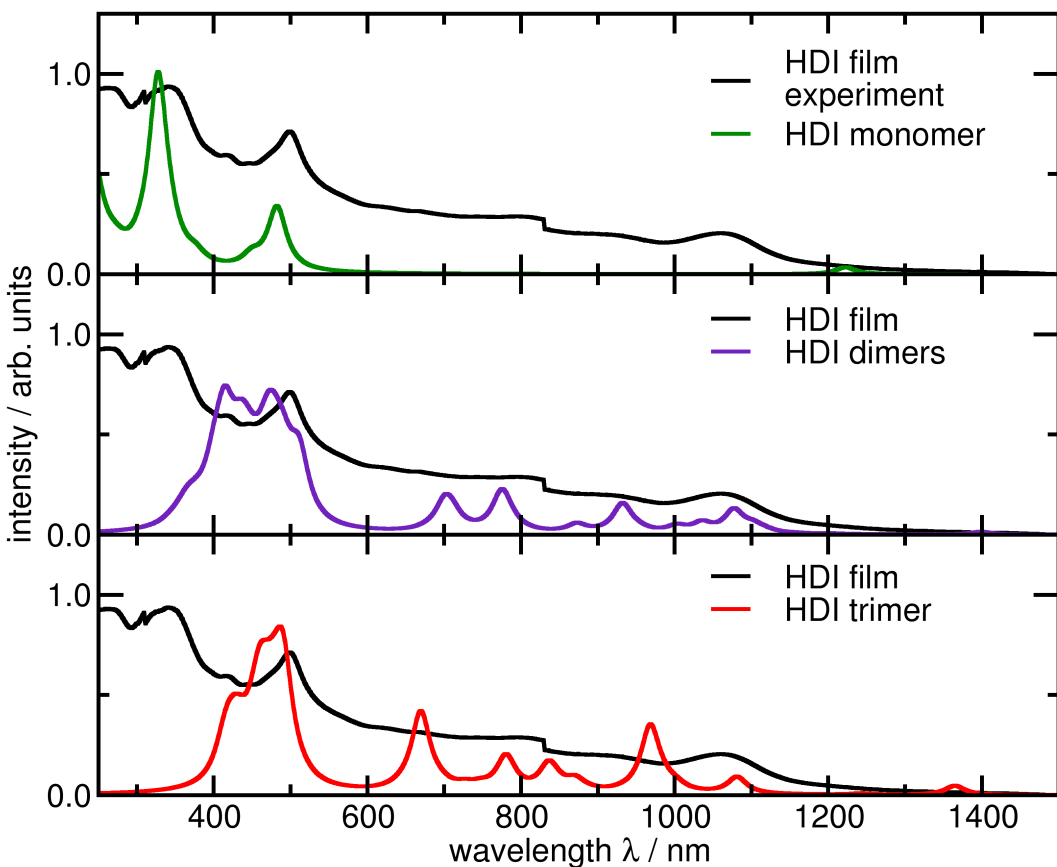


Figure 5.14: Experimental UV-Vis-NIR absorption spectra in a thin HDI film and theoretical TDDFT absorption spectra for HDI monomer, dimers and trimer at the optimised S<sub>0</sub> ground state geometry in CHCl<sub>3</sub> solution on PBE0-D3(BJ)/6-31G\* level. The dimer spectrum is generated by taking the arithmetic average of HDI dimer spectra for structures A, B, and C, assuming the same contribution of all conformation in the thin film to the overall absorption spectrum.

In the same way, a HDI trimer conformation is obtained, consisting of three stackable HDI monomers (Fig. 5.13). The trimer shows a  $\pi$ -stacking of the aromatic system in a screw-like manner. The relative orientation of two HDI molecules can be quantified by the dihedral angle  $\theta_1(N_{a1}-N_{a2}-N_{b1}-N_{b2}) = 25.3^\circ$  for monomer *a* and *b*,  $\theta_2(N_{b1}-N_{b2}-N_{c1}-N_{c2}) = -25.7^\circ$  for *b* and *c*, respectively. The monomer *c* is rotated relative to the monomer *a* with a dihedral angle  $\theta_3(N_{a1}-N_{a2}-N_{c1}-N_{c2}) = -51.1^\circ$ . In this index notation *a*, *b*, and *c* denote the individual HDI monomers in the trimer configuration, and the numbers refer to the nitrogen atoms.

The HDI trimer conformation displays the general trend towards accumulation of HDI monomers in screw-like aggregates, as the relative orientation of two adjacent HDI monomers in the trimer coincides with the alignment in dimer A-HDI. The HDI trimer binding energy is  $\Delta E_B = -4.08$  eV, which is evaluated according to the energy of three isolated HDI monomers  $\Delta E_B = E_{\text{trimer}} - 3E_{\text{monomer}}$ , and it is about twice the binding energy  $\Delta E_B = -2.07$  eV of A-HDI. This finding supports the tendency to form ordered aggregates in the thin film.

**Spectral Properties of Aggregates** The experimental UV-Vis-NIR absorption spectrum of HDI shows a broad band at 800 – 1000 nm in solution (Fig. 5.12). The spectrum of a thin film clearly reveals a noticeable red-shift in the long wavelength region and additionally continuous bands in the range of 600 – 1000 nm arise (Fig. 5.14). These characteristic absorption motives cannot originate from individual, isolated HDI monomers, but in return can be identified in the absorption spectra for HDI dimers and the HDI trimer stack, as they exhibit additional bands in the wavelength range between 600 – 1100 nm. The decomposition of the overall dimer spectrum into the individual contributions of the different dimer configurations (SI Fig. S11 [395]) demonstrates that the dimers A, B, C are responsible for the 650 – 830 nm, 900 – 1000 nm, and 1000 – 1150 nm wavelength range, respectively. These spectral features emerge as a result of the enhanced intermolecular interaction in the  $\pi$ -stacking HDI aggregates, that are built up during the solvent evaporation process. In addition, C-HDI dimer and the HDI trimer have smaller absorption bands in the long-wavelength range. All in all, the formation of  $\pi$ -stacking aggregated arrangements of HDI monomers can clarify the additional spectral properties in a thin HDI film (Fig. 5.14), which arise additionally in comparison to the absorption spectrum in  $\text{CHCl}_3$  solution (Fig. 5.12).

## 5.5 PDTTI

**Structure** The PDTTI acceptor molecule contains two PDI units linked by a three-element thiophene bridge (Fig. 5.1,9). We identified two enantiomers cis-PDTTI-A and cis-PDTTI-B. The chiral molecules differ in the relative orientation of the PDI subunits. A selection of characteristic structural parameters is defined visually for cis-PDTTI-A in Figure 5.15, e.g. the dihedral angle  $\theta_1$ , and the interatomic distances  $d_1$ ,  $d_2$ , and  $d_3$ . The optimised ground state  $S_0$  geometries in  $\text{CHCl}_3$  solution are depicted in Fig. 5.15. The structure cis-PDTTI-B is  $\Delta E_{\text{rel}} = 0.01$  eV lower in energy than the cis-PDTTI-A structure, so the enantiomers are considered energetically degenerated. The dihedral angles  $\theta_A=130.9^\circ$  and  $\theta_B=-135.7^\circ$  display the relative orientation of the PDI subunits in the enantiomers cis-PDTTI-A and cis-PDTTI-B. More characteristic structural parameters are summarised in Table A.9. The carbon-carbon distance  $d_1 \approx 2.8$  Å represents the relative packing distance in the intramolecular PDI-PDI stack, which is limited by the poly-thiophene groups acting as spacers.

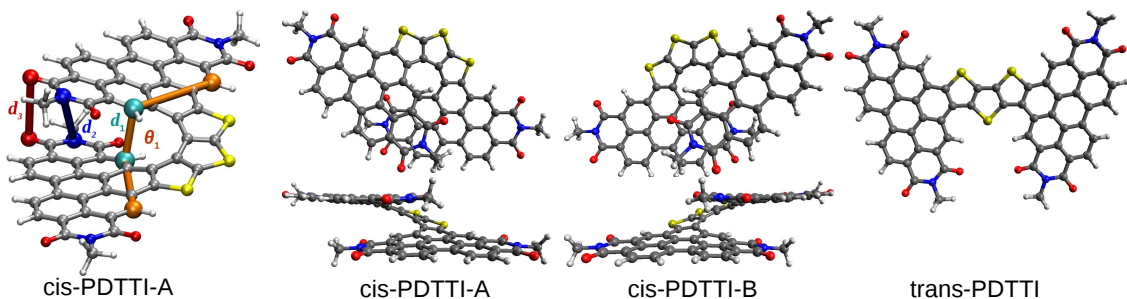


Figure 5.15: Visual definition of structural parameters in cis-PDTTI-A (left) including dihedral angle  $\theta_1$  (orange), interatomic distances  $d_1$  (cyan),  $d_2$  (blue), and  $d_3$  (red). Optimised ground state  $S_0$  geometries for the enantiomers cis-PDTTI-A and cis-PDTTI-B and the planar trans-PDTTI on PBE0-D3(BJ)/6-31G\* level in  $\text{CHCl}_3$  solution.

**Spectral Properties** The optical properties of PDTTI were investigated by UV-Vis absorption spectroscopy. As shown in Figure (5.16,i), PDTTI exhibits three absorption bands in the range 300 – 600 nm with three maxima at 303 nm, 360 nm, and 494 nm in dilute chloroform solution. The two enantiomers cis-PDTTI-A and cis-PDTTI-B yield indistinguishable TDDFT absorption spectra in  $\text{CHCl}_3$  solution. The frontier orbitals and associated Kohn-Sham energies are displayed in Fig. 5.20. Most frontier orbitals, such as HOMO and LUMO, possess contributions at both PDI units and the thiophene bridge. According to the TDDFT eigenvectors for cis-PDTTI-A (5.16,i), the lowest energy band arises from several excitations like the lowest excited singlet state  $S_1$  with a 97% HOMO-LUMO contribution, the  $S_4$  excitation with a 75.3% HOMO-2 to LUMO contribution and the  $S_5$  excitation with 83.6% HOMO-1 to LUMO+1 contribution, respectively. The band at 360 nm arises predominantly due to the  $S_9$  state containing a significant transition from HOMO-3 to LUMO+1 with a 93.8% weight. The highest energy band (303 nm) can be assigned to the  $S_{46}$  and  $S_{60}$  excited states. The former state primarily involves transitions from the HOMO-2 to the LUMO+4 with a weight of 40.4%. The latter state has a 20.3% contribution from the HOMO-16 to LUMO+1 transition and from the HOMO-14 to the LUMO+1 with a weight of 19.4%. The involved transitions are similar for cis-PDTTI-A and cis-PDTTI-B for the lower energy excitations  $S_1$  to  $S_{10}$ , and the contributions distinguish slightly, whereas the orbital order can differ for higher-energy transitions.

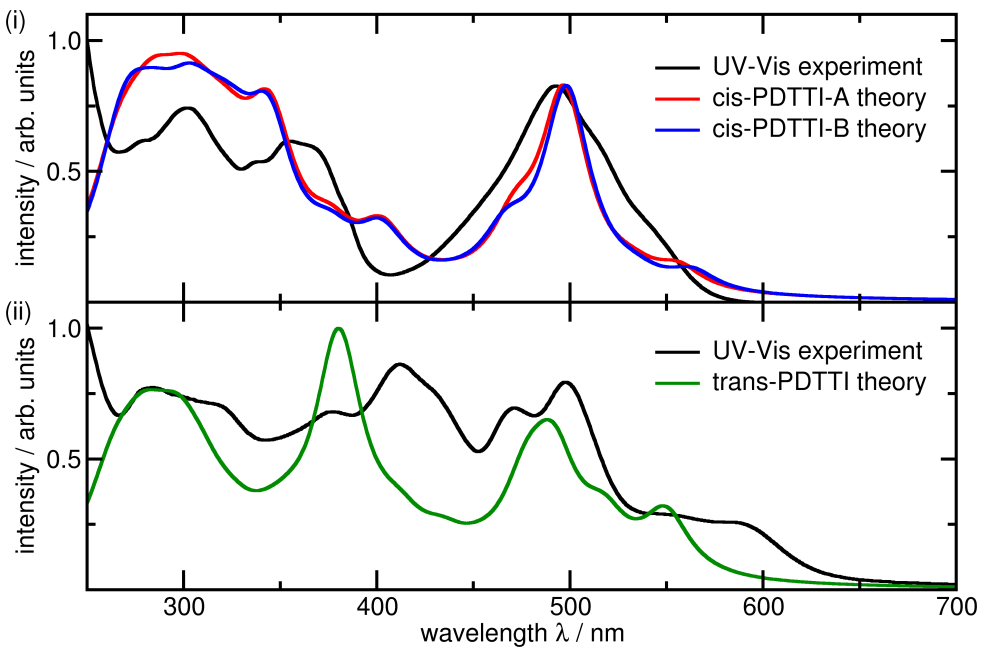


Figure 5.16: Experimental UV-Vis spectra for cis-PDTI and (i) TDDFT absorption spectra for enantiomers cis-PDTI-A (red), cis-PDTI-B (blue) and (ii) trans-PDTI (green) on PBE0-D3(BJ)/6-31G\* level in CHCl<sub>3</sub> solution.

The trans-PDTI molecule has a planar geometry with three alternating sulfur atoms in the bridge (Fig. 5.15). The experimental UV-vis spectrum of trans-PDTI has three prominent absorption peaks at 592 nm, 497 nm and 412 nm (Fig. 5.16,ii). The low-wavelength peak in the TDDFT spectrum for trans-PDTI is dominated by the S<sub>1</sub> excitation. It is mainly determined by the  $\pi$ - $\pi^*$ -character of the HOMO to LUMO transition with a contribution of 94.9%. The HOMO-1 to LUMO transition dominates the S<sub>3</sub> state with a contribution of 91.5%. The highest oscillator strength  $f = 1.33$  is found for the S<sub>9</sub> excitation in trans-PDTI with a 90.6% HOMO to LUMO contribution.

The enantiomers can be distinguished in the experimental CD spectra (Fig. 5.17). The theoretical electronic circular dichroism spectra coincide with the experimental data, especially in the lower energy regime, as both enantiomers cause mirrored spectra. Hence, the experimental spectrum A is associated with the theoretical ECD spectrum of cis-PDTI-A and experiment B originates from structure cis-PDTI-B. All spectral CD features cancel in a racemate containing 50% cis-PDTI-A and 50% cis-PDTI-B structures. The optical energy gaps  $\Delta E_g$  and frontier orbital energy levels do not differ significantly for the enantiomers cis-PDTI and trans-PDTI (Tab. 5.3).

Table 5.3: HOMO energy  $E_{\text{HOMO}}$ , LUMO energy  $E_{\text{LUMO}}$  and optical energy gap  $\Delta E_g$  in eV for cis-PDTI-A, cis-PDTI-B and trans-PDTI at the optimised S<sub>0</sub> ground state geometry in CHCl<sub>3</sub>.

	$E_{\text{HOMO}} / \text{eV}$	$E_{\text{LUMO}} / \text{eV}$	$\Delta E_g / \text{eV}$
cis-PDTI-A	-6.12	-3.40	2.72
cis-PDTI-B	-6.12	-3.42	2.70
trans-PDTI	-6.10	-3.36	2.74

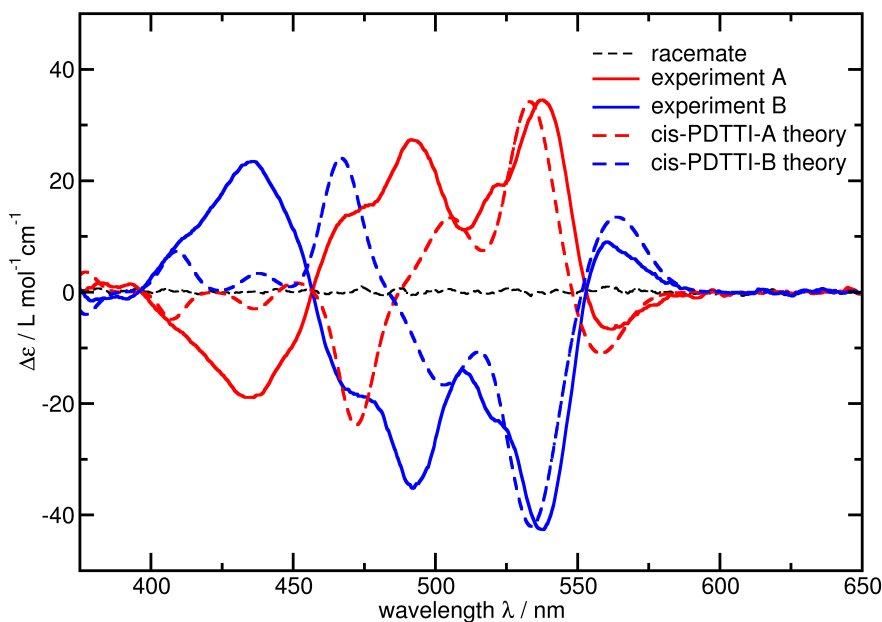


Figure 5.17: Experimental CD spectra for cis-PDTTI and theoretical ECD spectra for enantiomers cis-PDTTI-A and cis-PDTTI-B on PBE0-D3(BJ)/6-31G\* level in CHCl<sub>3</sub> solution.

**Aggregation and Charge Transfer Properties** Ground state S<sub>0</sub> geometry optimisations on PDTTI dimers give rise to six distinct aggregation configurations, labelled A to F, for cis-PDTTI-A. They are ordered according to the relative total energy  $E_{\text{rel}}$  (Fig. 5.18). Dimer A-cis-PDTTI exhibits an interlaced, spiral-like aggregation, with an extended intermolecular  $\pi$ -stacking pattern and possesses the lowest total energy. Dimer C-cis-PDTTI has similar orientation as dimer A-cis-PDTTI, but it exhibits a small lateral shift. In dimer B-cis-PDTTI and D-cis-PDTTI, we find a slipped stacking, where two PDI-subunits are rotated with respect to each other at rotatory dihedral angles  $\theta(N_1^{36}-N_1^{45}-N_2^{27}-N_2^{52}) = 53.4^\circ$  and  $\theta(N_1^{36}-N_1^{45}-N_2^{27}-N_2^{52}) = 67.9^\circ$ , respectively. The subscripts for the nitrogen atoms refer to monomer 1 and 2 in the dimer configuration, and the superscript number refers to the atomic index. Dimer E-cis-PDTTI has a spiral-like stacking structure and in dimer F-cis-PDTTI two PDI-subunits stack with a lateral shift.

Furthermore, we obtain seven dimer configurations for trans-PDTTI labelled A to G (Fig. 5.19). Trans-PDTTI molecules favour a planar, parallel orientation of the monomers, with a small lateral shift (A-trans-PDTTI). In contrast, the monomers in B-trans-PDTTI show an anti-parallel orientation. The monomers in C-trans-PDTTI are parallel oriented and laterally shifted with respect to A-trans-PDTTI. We also find a lateral shift for the monomers in D-trans-PDTTI concerning B-trans-PDTTI, where both dimers hold a planar, anti-parallel orientation. The monomers are rotated by an angle of  $\theta(N_1^{36}-N_1^{45}-N_2^{27}-N_2^{52}) = 66.3^\circ$  to each other in E-trans-PDTTI. Dimer F-trans-PDTTI shows a lateral stacking. The dimer configuration G yields two interlaced monomers, and it is the energetically highest structure concerning the set of dimer configurations considered.

The internal reorganization energy is  $\lambda_{\text{in}}^{\text{h}} = 0.108$  eV for hole transfer between cis-PDTTI dimers, but  $\lambda_{\text{in}}^{\text{h}} = 0.142$  eV is higher for transfer between trans-PDTTI dimers (B3LYP-D3(BJ)/6-31G\*). The internal reorganization energy is  $\lambda_{\text{e}}^{\text{in}} = 0.146$  eV for electron transfer between cis-PDTTI dimers and reduced to  $\lambda_{\text{e}}^{\text{in}} = 0.126$  eV for transfer between trans-PDTTI dimers.

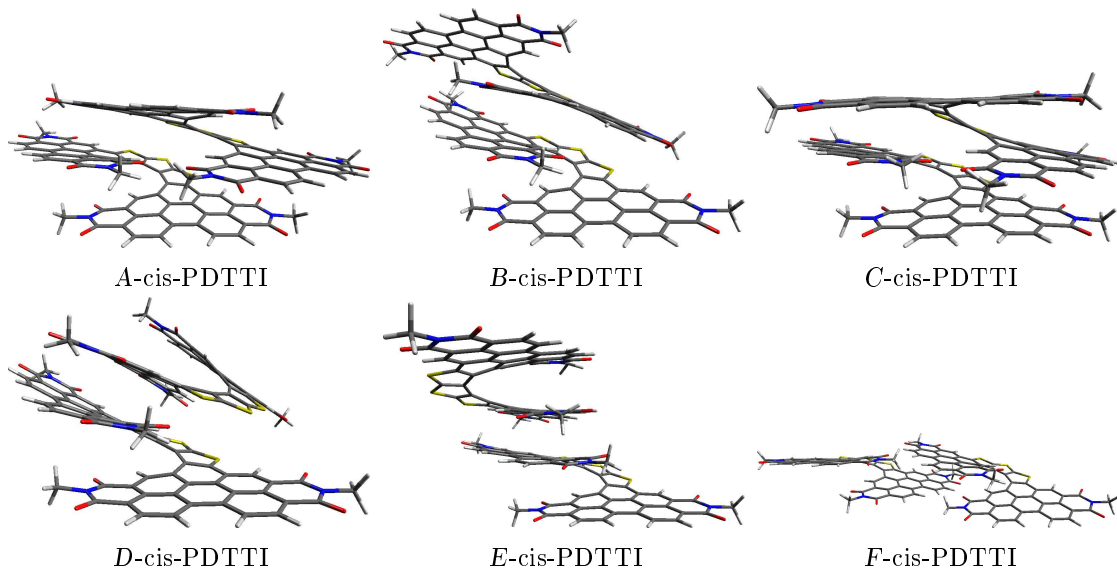


Figure 5.18: Optimised ground state  $S_0$  geometries of stacking aggregates for cis-PDTI-A on B3LYP-D3(BJ)/6-31G\* level of theory. The dimer structures are labelled with A to F.

Table 5.4 summarises the DIPRO-based  $|J_{AB}^h|$  and  $|J_{AB}^e|$ , as well as the Marcus rates  $k_{AB}^h$  and  $k_{AB}^e$  ordered by the relative energy  $E_{\text{rel}}$  for all investigated aggregation patterns of PDTI. Both the  $|J_{AB}^h|$  and  $|J_{AB}^e|$  are in the same order of magnitude of  $|J_{AB}| \approx 10^{-2}$  eV for all aggregation patterns of cis-PDTI. C-cis-PDTI yields the largest  $|J_{AB}^h| = 8.28 \times 10^{-2}$  eV, which is also favourable for a high Marcus rate of  $k_{AB}^h = 2.82 \times 10^{13}$  s $^{-1}$ . A-cis-PDTI performs similarly well for holes due to the structural similarity. The highest value of  $|J_{AB}^e| = 8.38 \times 10^{-2}$  eV also leads to the highest rate for D-cis-PDTI with  $k_{AB}^e = 2.11 \times 10^{14}$  s $^{-1}$  of all cis-PDTI structures. All other cis-PDTI aggregates yield electron rates at the order of  $k_{AB}^e \approx 10^{13}$  s $^{-1}$ , even the energetically unfavourable structure F-cis-PDTI. The number of adjoining PDI units, i.e. whether one or two units form  $\pi$ -interactions, does not appear to significantly influence the charge transfer properties for the aggregate structures investigated. For example, E-cis-PDTI with only a single PDI-PDI interface has the smallest  $|J_{AB}^h|$  and  $k_{AB}^h$ , but  $|J_{AB}^e|$  and  $k_{AB}^e$  are surprisingly good. In comparison, the values of A, B and C with two interfaces do not clearly stand out positively from those with only one, as in D, E, F.

Due to the planarity of trans-PDTI, which is favourable for a sizeable  $\pi$ -stacking interaction volume, we obtain high charge transfer integrals  $|J_{AB}^h|$  and  $|J_{AB}^e|$  for the aggregates A, B, C, and D. Consequently, the Marcus rates for holes  $k_{AB}^h$  and especially for electrons  $k_{AB}^e$  are also increased for these structures. D-trans-PDTI yields the most enormous rates  $k_{AB}^h$  and  $k_{AB}^e$  due to the planar and anti-parallel alignment of the monomers. Even the interlaced monomers in G-trans-PDTI are suitable for electron transfer. The relative rotation of the monomers against each other in E and F leads to a reduction of  $|J_{AB}^h|$  and  $|J_{AB}^e|$ , which significantly downscals  $k_{AB}^e$  in particular.

If one averages the values for all dimers, then cis-PDTI dimers yield  $|\bar{J}_{AB}^h| = (5.20 \pm 2.40) \times 10^{-2}$  eV and similar values for electron transfer  $|\bar{J}_{AB}^e| = (4.37 \pm 2.20) \times 10^{-2}$  eV. The corresponding values for trans-PDTI  $|\bar{J}_{AB}^h| = (9.77 \pm 6.71) \times 10^{-2}$  eV and  $|\bar{J}_{AB}^e| = (6.84 \pm 6.78) \times 10^{-2}$  eV are higher than those for cis-PDTI, which can be attributed to the enhanced tendency to form  $\pi$ -aggregation in trans-PDTI (Tab. 5.4).

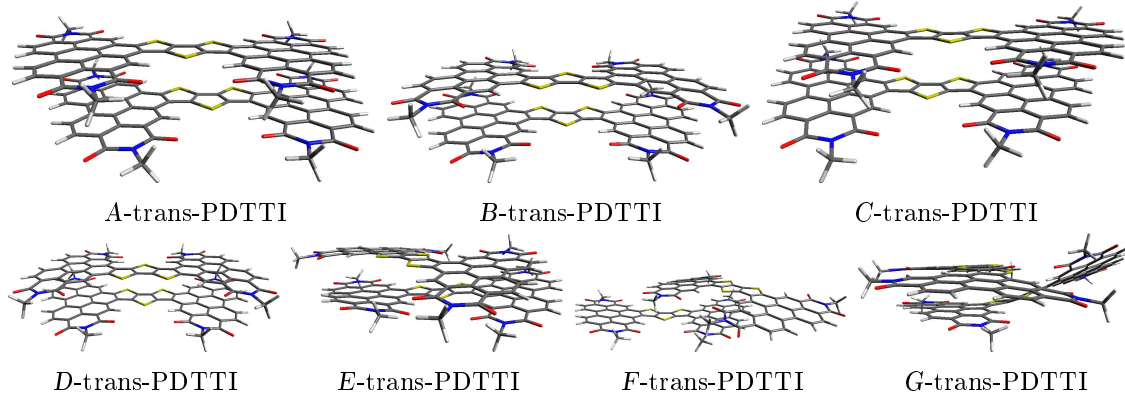


Figure 5.19: Optimised ground state  $S_0$  geometries of stacking aggregates for trans-PDTI on B3LYP-D3(BJ)/6-31G\* level of theory. The different dimer structures are labelled with *A* to *G*.

Though one finds higher charge transfer integrals and favourable lower internal reorganization energies for hole transfer than for electron transfer, the resulting averaged Marcus rates for electrons transfer  $\bar{k}_{AB}^e = (7.13 \pm 7.27) \times 10^{13} \text{ s}^{-1}$  (cis-PDTI) and  $\bar{k}_{AB}^e = (2.13 \pm 3.02) \times 10^{14} \text{ s}^{-1}$  (trans-PDTI) are higher than those for hole transfer  $\bar{k}_{AB}^h = (1.06 \pm 1.05) \times 10^{13} \text{ s}^{-1}$  (cis-PDTI), and  $\bar{k}_{AB}^h = (7.19 \pm 8.25) \times 10^{13} \text{ s}^{-1}$  (trans-PDTI). The reasons for this are contributions in the external field to the charge transfer rates. However, one should bear in mind that outer-sphere contributions are not included in these investigations on isolated dimer configurations.

All in all, both cis-PDTI and trans-PDTI have promising charge transfer properties for application in organic solar cells.

Table 5.4: Marcus charge transfer rates between optimised dimer structures for cis-PDTI and trans-PDTI for hole transfer  $k_{AB}^h$  and for electron transfer  $k_{AB}^e$  on B3LYP-D3(BJ)/6-31G\* level of theory. Furthermore the relative energies  $E_{\text{rel}}$  with respect to the most stable aggregation motive and the charge transfer integral  $|J_{AB}|$  based on DIPRO calculations are presented.

dimer conformation	$E_{\text{rel}} / \text{eV}$	$ J_{AB}^h  / \text{eV}$	$k_{AB}^h / \text{s}^{-1}$	$ J_{AB}^e  / \text{eV}$	$k_{AB}^e / \text{s}^{-1}$
<i>A</i> -cis-PDTI	0.000	6.66E-2	1.66E+13	4.09E-2	4.62E+13
<i>B</i> -cis-PDTI	0.042	4.59E-2	8.71E+12	3.31E-2	2.92E+13
<i>C</i> -cis-PDTI	0.254	8.28E-2	2.82E+13	2.09E-2	1.17E+13
<i>D</i> -cis-PDTI	0.441	5.42E-2	8.64E+12	8.38E-2	2.11E+14
<i>E</i> -cis-PDTI	0.488	1.10E-2	2.61E+11	5.08E-2	8.49E+13
<i>F</i> -cis-PDTI	1.226	5.12E-2	1.11E+12	3.25E-2	4.47E+13
<i>A</i> -trans-PDTI	0.000	1.78E-1	1.60E+14	8.65E-2	1.91E+14
<i>B</i> -trans-PDTI	0.046	1.74E-1	1.72E+14	1.62E-1	6.27E+14
<i>C</i> -trans-PDTI	0.051	6.59E-2	2.21E+13	7.61E-2	1.47E+14
<i>D</i> -trans-PDTI	0.080	1.78E-1	1.79E+14	1.65E-1	6.49E+14
<i>E</i> -trans-PDTI	0.893	7.81E-2	3.33E+13	2.01E-3	9.90E+10
<i>F</i> -trans-PDTI	1.660	4.02E-2	2.72E+12	1.06E-3	4.41E+10
<i>G</i> -trans-PDTI	1.689	2.79E-2	2.85E+12	5.35E-2	8.60E+13

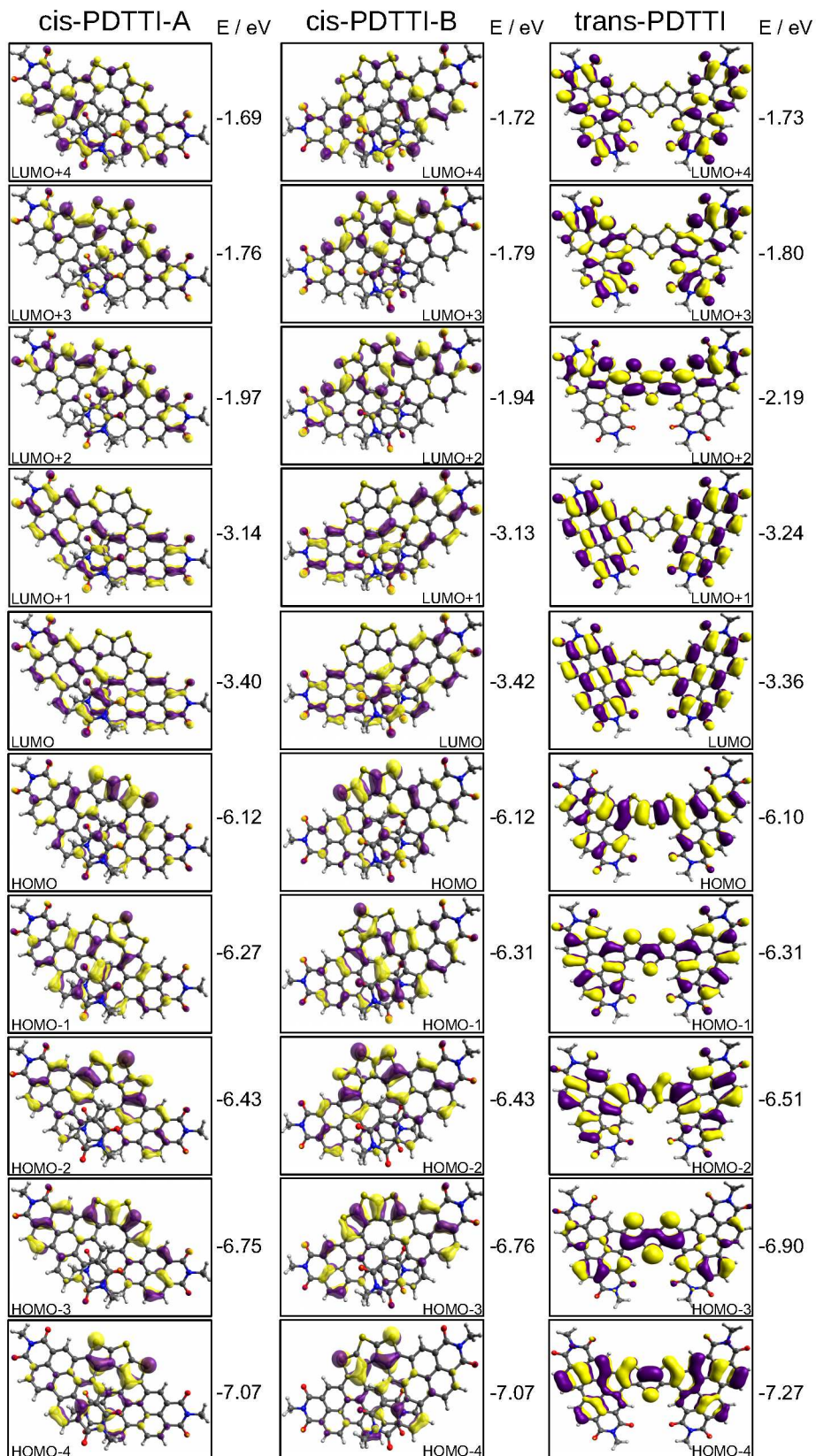


Figure 5.20: Frontier orbitals and Kohn-Sham orbital energies for the enantiomers cis-PDTTI-A, cis-PDTTI-B and trans-PDTTI on PBE0-D3(BJ)/6-31G\* level in CHCl<sub>3</sub> solution.

## 5.6 PHHP-AS

We determine the molecular structure, the chirality, spectral properties, aggregation and charge transfer properties of the PHHP-AS (Fig. 5.1,10). The molecule contains a helicene linking two perylene diimide groups. For simplicity, we abbreviate PHHP-AS as PHHP and use the suffix (*M*, *P*) to distinguish enantiomers and the prefix (*A*–*F*) for aggregation motives.

**Structure** Two PHHP-AS enantiomers are obtained in DFT-based geometry optimisations, which are labelled *P* for positive, clockwise orientation of the PDI units and *M* for minus, counter-clockwise orientation. The optimised ground state  $S_0$  geometries for PHHP in  $\text{CHCl}_3$  solution are depicted in Fig. 5.21. Both enantiomers PHHP-*P* and PHHP-*M* possess similar total energy. Some characteristic structural parameters are defined visually in Fig. 5.22 and summarised in Tab. A.10. The dihedral angles  $\theta_1^P = 20.57^\circ$  and  $\theta_1^M = -20.57^\circ$  describe the relative orientation of both PDI units. The same holds for  $\theta_2^P = 14.66^\circ$  and  $\theta_2^M = -14.66^\circ$ . So the PDI units are not oriented parallel to each other but form an acute angle. The distances  $d_1 = 3.39 \text{ \AA}$  and  $d_2 = 3.21 \text{ \AA}$  describe the intramolecular  $\pi$ -stacking distance for two carbon atoms that are aligned on top of each other in the next carbon 'grid'-layer (see Figures 5.21,ii and 5.22,i for comparison). The distance  $d_3$  (red) is defined between the inner oxygen atoms on the PDI units and similar for both enantiomers.

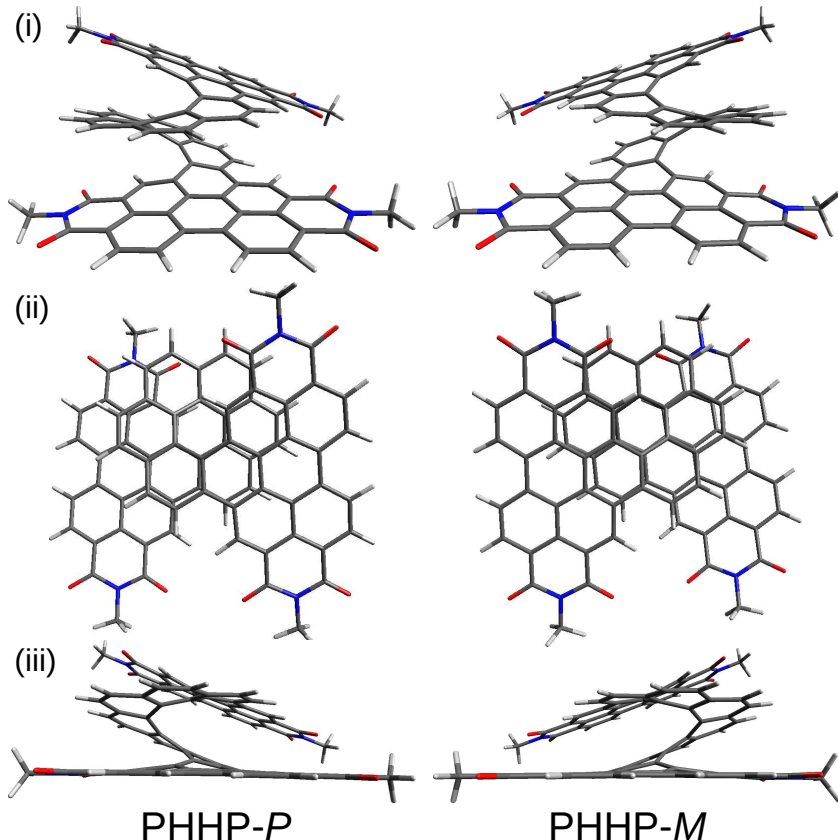


Figure 5.21: Optimised ground state  $S_0$  geometries for the enantiomers PHHP-*P* and PHHP-*M* on PBE0-D3(BJ)/6-31G\* level in  $\text{CHCl}_3$  solution. (i) side view, (ii) top view, (iii) in-plane view.

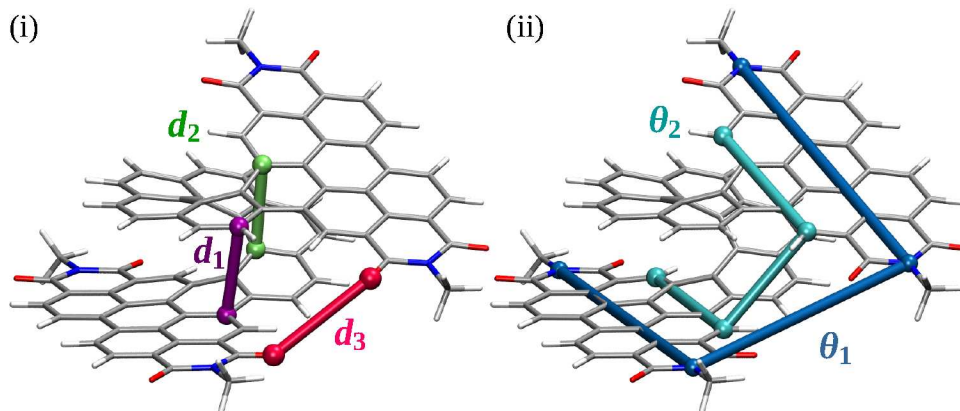


Figure 5.22: Visual definition of characteristic structure parameters for the optimised ground state  $S_0$  geometries for PHHP-*P*. (i) The intramolecular distance for the PDI stacks is characterised with the distances  $d_1$ (violet) and  $d_2$ (green). The distance  $d_3$ (red) is between the inner oxygen atoms in the PDI units. (ii) The dihedral angles  $\theta_1$ (blue) and  $\theta_2$ (cyan) take the relative orientation of the PDI units into account.

**Spectral Properties** The optical properties of PHHP were investigated by UV-Vis absorption spectroscopy and compared to TDDFT absorption spectra (Fig. 5.23). The experimental absorption spectrum gives rise to two significant bands in the range 250 nm to 550 nm. The first band is in the range between 550 nm and 575 nm and the second band is in the range between 250 nm and 350 nm. Both enantiomers PHHP-*P* and PHHP-*M* give rise to similar theoretical absorption spectra (Fig. 5.23,i).

The first  $S_1$  excitation at 560 nm is dominated by a HOMO to LUMO transition with an 82.5% contribution. This transition exhibits a  $\pi-\pi^*$ -character at the PDI units (Fig. A.28). The lowest energy band can be assigned to the  $S_4$  and  $S_6$  excited states. The former involves transitions primarily from the HOMO-1 to the LUMO+1 with a weight of 88.7%, while the latter has a 79.7% contribution from the HOMO-2 to LUMO transition and from the HOMO to the LUMO with a weight of 14.1%. The  $S_1$ ,  $S_4$  and  $S_6$  excitations of the TDDFT calculations can reproduce the double-peak structure of the low-energy band in the experiment with a minimal red shift. This is valid even though the first peak is only present as a flank in the theoretical spectrum due to the small oscillator strength  $f = 0.12$  of the  $S_1$  excitation.

The highest energy band arises from several excitations like the excited singlet state  $S_{35}$  with a 21.9% HOMO-7 to LUMO+1 contribution and a 27.2% HOMO-1 to LUMO+5 contribution and the  $S_{66}$  excitation with a 14.3% HOMO-18 to LUMO contribution and with 31.5% HOMO-2 to LUMO+8 contribution, respectively.

TDDFT absorption spectra were averaged for different aggregates (*A–F*, see below) for both *P* and *M* enantiomers in CHCl<sub>3</sub> solution, and exhibit the same spectral features as the monomer components (Fig. 5.23,ii). Therefore, additional absorption bands are not expected in the experimental spectrum of a thin film of PHHP-AS caused by intermolecular interactions.

The experimental ECD spectra can be assigned to the PHHP conformations *P* and *M* (Fig. 5.24). The positive Cotton effect in the long-wave region of the experimental CD spectrum A, is also found in the ECD spectrum of the enantiomer PHHP-*P*. Similarly, we can associate the negative Cotton effect in experiment B with that in the ECD spectrum of PHHP-*M*.

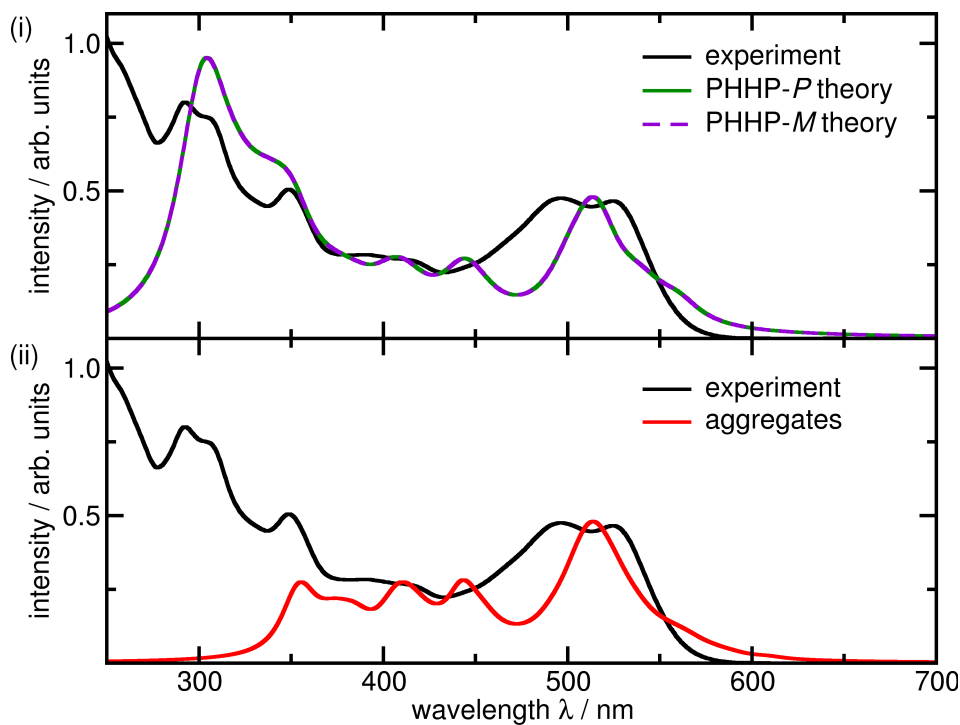


Figure 5.23: Experimental UV-Vis spectrum for PHHP and (i) TDDFT absorption spectra for PHHP as the *P* (green), *M* (violet) enantiomer and (ii) TDDFT spectrum from stacking aggregates consisting of PHHP-*P* and PHHP-*M* aggregates (*A*–*F*) in CHCl<sub>3</sub> solution on PBE0-D3(BJ)/6-31G\* level of theory. The PHHP aggregates exhibit the same spectral features as the monomers.

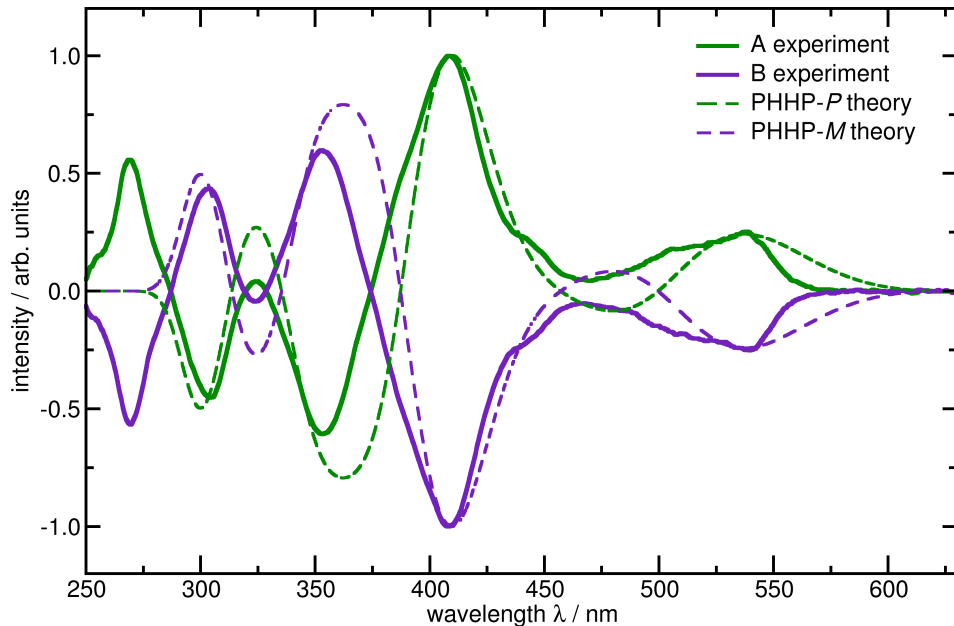


Figure 5.24: Experimental CD spectra (A, B) for PHHP and ECD spectra for PHHP as the *P* (green), *M* (violet) enantiomer in CHCl<sub>3</sub> solution on PBE0-D3(BJ)/6-31G\* level of theory.

Both enantiomers PHHP-*P* and *M* give rise to the same frontier orbital energies like HOMO energy  $E_{\text{HOMO}} = -5.99$  eV, LUMO energy  $E_{\text{LUMO}} = -3.20$  eV, which results in an optical gap energy  $\Delta E_g = 2.787$  eV (Fig. A.28). The reorganization energy for electron transfer  $\lambda_e^{\text{in}}$  in PHHP is slightly lower than for hole transfer  $\lambda_h^{\text{in}}$ , which is beneficial for higher Marcus rates for electron (Tab. A.11).

**Aggregation and Charge Transfer Rates** Geometry optimisations on PHHP dimers lead to six distinct aggregation patterns in conformation *P* (Fig. 5.25) and in conformation *M* (Fig. 5.26). The different dimer structures are labelled *A* to *F*.

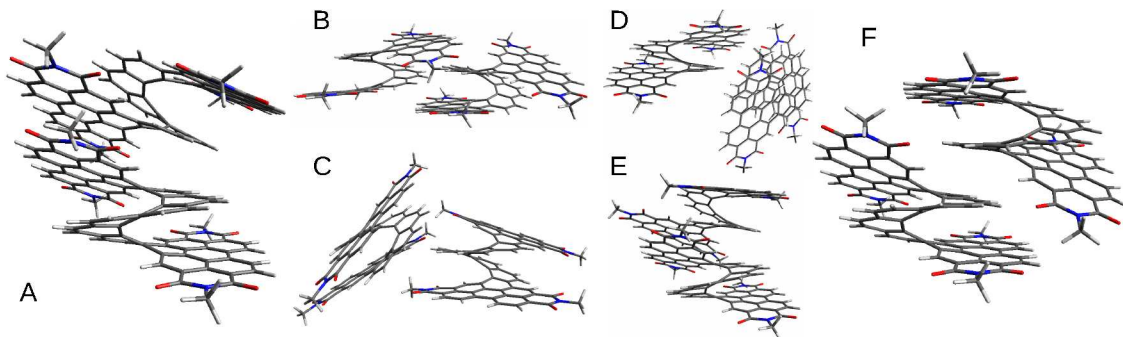


Figure 5.25: Optimised ground state geometries of stacking aggregates for PHHP in *P* conformation in CHCl<sub>3</sub> solution on PBE0-D3(BJ)/6-31G\* level of theory. The different dimer structures are labelled *A* to *F*.

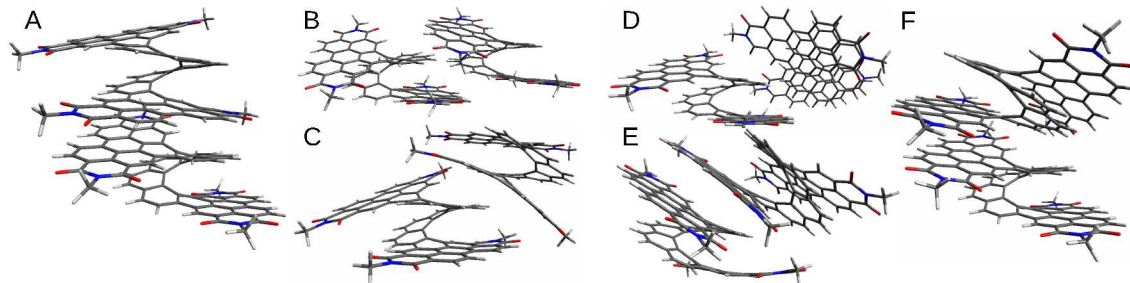


Figure 5.26: Optimised ground state geometries of stacking aggregates for PHHP in *M* conformation in CHCl<sub>3</sub> solution on PBE0-D3(BJ)/6-31G\* level of theory. The different dimer structures are labelled *A* to *F*.

The right-handed, spiral PHHP forms several distinct stacking arrangement patterns. *A*-PHHP-*P* makes a slipped, face-on stack with two PDI units aligned nearly parallel to each other. *B*-PHHP-*P* forms a lateral arrangement in which the molecules have a displacement of about 10.5 Å relative to each other. *C*-PHHP-*P* and *D*-PHHP-*P* are T-stacks with a side-shifted arrangement. The lowest energy aggregation pattern is *E*-PHHP-*P*, which builds a right-handed helical arrangement. *F*-PHHP-*P* is a symmetrical arrangement like a slipped lateral aggregation.

The aggregates *A*-PHHP-*M* and *F*-PHHP-*M* form a left-handed helical supramolecular structures. *A*-PHHP-*M* has the more natural continuation due to the co-facial alignment, which can also be seen from the more favourable energy  $E_{\text{rel}}$ . *B*-PHHP-*M* is a laterally shifted arrangement, with a similar shift as in the *B*-PHHP-*P* arrangement.

A slipped overlaying displacement is found in *C*-PHHP-*M*. *D*-PHHP-*M* forms a laterally shifted T-stack in which the two molecules are approximately orthogonal to each other. *E*-PHHP-*M* has a shifted helical arrangement.

The comparison of the relative energies  $E_{\text{rel}}$  shows that the aggregates *E*-PHHP-*P* and *A*-PHHP-*M* are the most stable structures (Tab. 5.5). Both demonstrate a  $\pi$ -stacking motive of neighbouring PDI units and a supramolecular extension of the helical structure, as expected for aggregations with a higher number of molecules.

The helical aggregation favours enhanced electronic couplings since both enantiomers have the largest transfer integrals  $|J_{AB}^h|$  and  $|J_{AB}^e|$  in the respective set of aggregation patterns. This is also reflected in high Marcus rates for *E*-PHHP-*P* and *A*-PHHP-*M*. Moreover, both structures exhibit higher Marcus charge transfer rate for electron transport  $k_{AB}^e = 1.20 \times 10^{13} \text{ s}^{-1}$  for *E*-PHHP-*P* and  $k_{AB}^e = 1.62 \times 10^{14} \text{ s}^{-1}$  for *A*-PHHP-*M* than for hole transfer  $k_{AB}^h = 4.93 \times 10^{12} \text{ s}^{-1}$  and  $k_{AB}^h = 3.64 \times 10^{12} \text{ s}^{-1}$ , respectively.

Due to the structural similarity, also *A*-PHHP-*P* and *F*-PHHP-*M* provide good charge transfer properties. The T-stacks *C* and *D* tend to deliver lower values. The *B*-aggregates with lateral displacement are more suitable for electron transfer than for hole transfer.

On average the PHHP aggregation patterns yield higher charge transfer integrals for holes  $|\bar{J}_{AB}^h| = (2.17 \pm 1.89) \times 10^{-2} \text{ eV}$  than for electrons  $|\bar{J}_{AB}^e| = (8.05 \pm 7.77) \times 10^{-3} \text{ eV}$  in PHHP-*P*. This finding also holds for PHHP-*M* with  $|\bar{J}_{AB}^h| = (2.61 \pm 1.42) \times 10^{-2} \text{ eV}$  and  $|\bar{J}_{AB}^e| = (2.56 \pm 2.47) \times 10^{-2} \text{ eV}$ . However, both enantiomers favour electron transfer, as  $\bar{k}_{AB}^e = (3.69 \pm 2.16) \times 10^{12} \text{ s}^{-1}$  in PHHP-*M* exceeds  $\bar{k}_{AB}^h = (1.36 \pm 1.92) \times 10^{12} \text{ s}^{-1}$  in PHHP-*P*, and slightly exceeds  $\bar{k}_{AB}^h = (1.35 \pm 1.13) \times 10^{12} \text{ s}^{-1}$  in PHHP-*M*.

In conclusion, we investigated the structural features of PHHP enantiomers, their spectral characteristics and their aggregation based on dimer structures. We linked their arrangements to charge transfer properties. Our data suggest that the packing of PHHP molecules forming supramolecular, helical arrays, yields high potential for efficient electron transport.

Table 5.5: Marcus charge transfer rates between optimised dimer structures for PHHP-*P* and PHHP-*M* for hole transport  $k_{AB}^h$  and for electron transport  $k_{AB}^e$  on B3LYP-D3(BJ)/6-31G\* level of theory. Furthermore, the relative energies are presented concerning the most stable aggregation, and the charge transfer integrals  $|J_{AB}|$  based on DIPRO calculations are given.

dimer conformation	$E_{\text{rel}} / \text{eV}$	$ J_{AB}^h  / \text{eV}$	$k_{AB}^h / \text{s}^{-1}$	$ J_{AB}^e  / \text{eV}$	$k_{AB}^e / \text{s}^{-1}$
<i>A</i> -PHHP- <i>P</i>	0.118	2.37E-2	1.09E+12	5.64E-3	9.12E+11
<i>B</i> -PHHP- <i>P</i>	1.297	1.05E-2	6.22E+10	1.45E-2	8.35E+12
<i>C</i> -PHHP- <i>P</i>	1.317	1.35E-3	9.47E+08	6.99E-4	1.97E+10
<i>D</i> -PHHP- <i>P</i>	1.391	7.35E-3	2.65E+10	3.20E-3	4.15E+11
<i>E</i> -PHHP- <i>P</i>	0.000	5.00E-2	4.93E+12	2.06E-2	1.20E+13
<i>F</i> -PHHP- <i>P</i>	0.958	3.70E-2	1.99E+12	3.64E-3	4.21E+11
<i>A</i> -PHHP- <i>M</i>	0.000	4.86E-2	3.64E+12	7.11E-2	1.62E+14
<i>B</i> -PHHP- <i>M</i>	1.390	1.30E-2	1.02E+11	1.46E-2	8.48E+12
<i>C</i> -PHHP- <i>M</i>	0.828	2.59E-2	7.17E+11	1.80E-4	1.15E+09
<i>D</i> -PHHP- <i>M</i>	1.377	9.26E-3	6.38E+10	6.04E-3	1.40E+12
<i>E</i> -PHHP- <i>M</i>	0.167	2.76E-2	1.54E+12	3.22E-2	3.03E+13
<i>F</i> -PHHP- <i>M</i>	0.167	3.23E-2	2.12E+12	2.84E-2	2.36E+13

## 5.7 Laddered Graphene Nanoribbons (PDI-Pyr)

The laddered graphene nanoribbons  $\text{PDI}_n\text{-Pyr}(n - 1)$  belong to the group of twistacenes, which are chiral acenes that exhibit a chiral rotatory structure [411]. In decatwistacene the structural stability of the helical conformation is maintained due to the steric hindrance between imide groups and neighbouring annulated benzene rings. The overall end-to-end torsion angle of about  $170^\circ$  was the highest reported until 2017 [411]. An octadecatwistacene with 18 acene units exceeded this result with  $305^\circ$  in 2019. Alternatively, the pyrene (Pyr) group can also bear an imide motive as in dodecatwistarene imides and form a twisted zig-zag conformation, which yields remarkable electron mobility of up to  $\mu = 1.5 \text{ cm}^2/\text{Vs}$  in OFETs [421].

An analogue construction pattern is applied to the laddered nanoribbons consisting of two building blocks like the PDI unit and the polycyclic aromatic hydrocarbon unit pyrene (Pyr) [422], which contains two attached bulky t-butyl side groups. The PDI and Pyr units are aligned in an alternating fashion to build the laddered graphene nanoribbons PDI2-Pyr1, PDI4-Pyr3 and PDI8-Pyr7 (see Fig. 5.1,11,12,13).

**Structure and Spectral Properties** In the following, we will discuss different optimised ground state  $S_0$  configurations for laddered graphene nanoribbons as PDI2-Pyr1, PDI4-Pyr3 and PDI8-Pyr7, which consist of PDI and Pyr units (Fig. 5.27).

PDI2-Pyr1 was obtained in a clockwise rotated *P*-PDI2-Pyr1 configuration and an anti-clockwise oriented *M*-PDI2-Pyr1 configuration. However, a third *T*-PDI2-Pyr1 configuration is 0.05 eV lower in energy, where both PDI units remain parallel, and the central aromatic rings in the Pyr unit are tilted at an angle about  $\alpha = 31^\circ$  with respect to the PDI planes.

Depending on the synthetic chemical route, the PDI4-Pyr3 molecule can have various conformations with different alignments of the building blocks. We obtain a twisted molecule *T*-PDI4-Pyr3 configuration with a zig-zag pattern (*P,P,M,M,M,M*). In this notation, *P* and *M* refer to the relative orientation of the aromatic rings in the linking bay-region between the PDI and Pyr unit. We use *P* and *M* as a prefix referring to the helicity of the entire molecule.

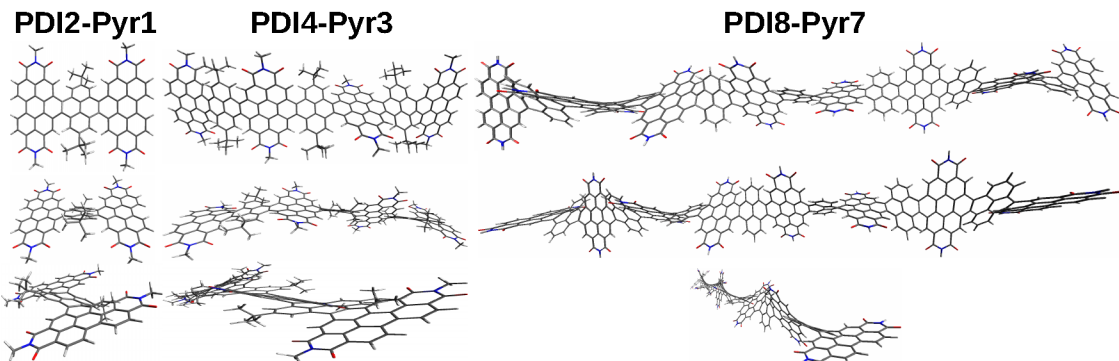


Figure 5.27: Optimised ground state geometries of *T*-PDI2-Pyr1, *T*-PDI4-Pyr3 and *P*-PDI8-Pyr7 on the DFT PBE0-D3(BJ)/6-31G\* level in  $\text{CHCl}_3$  solution. The PDI and Pyr components show twists of the aromatic subunits with respect to each other. *P*-PDI8-Pyr7 has a clockwise rotated helical structure.

Furthermore, we obtain an all *P*-PDI4-Pyr3 helix structure with a positive (clockwise) rotation of the subunits and a helix with a negative (anti-clockwise) orientation *M*-PDI4-Pyr3. The helical structures are about  $E = 0.965$  eV lower in energy than the *T*-PDI4-Pyr3 configuration. Both helical structures are basically equal in energy ( $\Delta E = 8$  meV). The *P*-PDI4-Pyr3 structure exhibits a torsion angle of  $\vartheta = 208^\circ$ , and *M*-PDI4-Pyr3 yields  $\vartheta = 211^\circ$ . The helices *P*-PDI4-Pyr3 and *M*-PDI4-Pyr3 are distinguishable due to their characteristic ECD spectra, where the *P* configuration gives rises to a positive Cotton effect and *M* to a negative (Fig. 5.28).

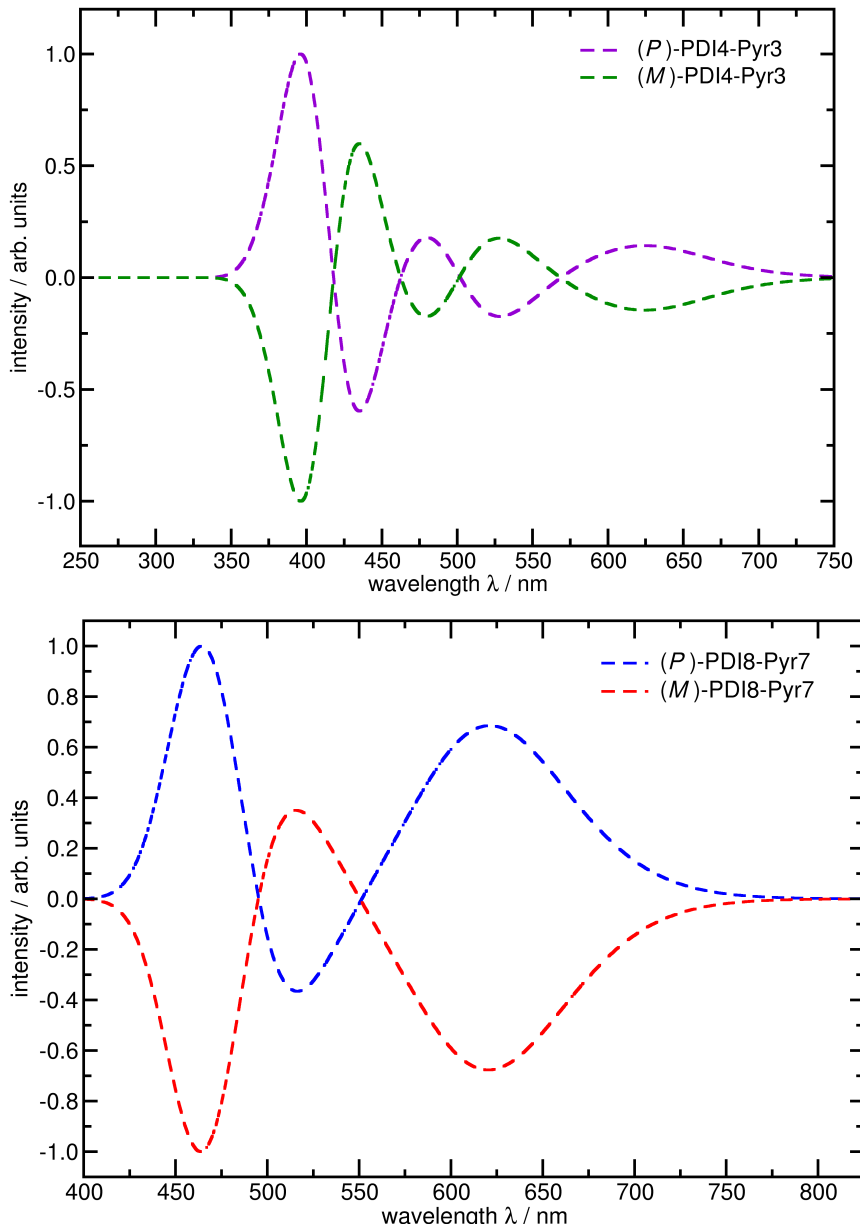


Figure 5.28: Normalised ECD spectra in a helical, clockwise-oriented *P*-PDI4Pyr3 (violet), an anti-clockwise-oriented *M*-PDI4Pyr3 (green) and helical *P*-PDI8Pyr7 (blue) and *M*-PDI8Pyr7 (red) in CHCl<sub>3</sub> solution on PBE0-D3(BJ)/6-31G\* level of theory. The underlying ECD calculations involve the  $N = 50$  lowest singlet states.

We can find three different conformations for the PDI8-Pyr7 laddered nanoribbons, which differ in the relative orientation of the PDI and Pyr units. The *P*-PDI8-Pyr7 is a helix turned clockwise, and it is similar in the total energy as the anti-clockwise oriented *M*-PDI8-Pyr7. Both helical conformations *P*-PDI8-Pyr7 and *M*-PDI8-Pyr7 possess a similar overall torsion angle of  $\vartheta = 391^\circ$  and  $\vartheta = 393^\circ$ , respectively. A similar twisted *T*-PDI8-Pyr7 structure yields a helical motive in some sections, but it exhibits some structural alternations in the Pyr subunit alignment and hence is about 0.4 eV higher in the total energy than the reference conformations *P* and *M*.

The helices *P*-PDI8-Pyr7 and *M*-PDI8-Pyr7 can be distinguished due to their ECD spectra (Fig. 5.28). *P*-PDI8-Pyr7 exhibits a positive Cotton effect for the highest wavelength absorption band, whereas *M*-PDI8-Pyr7 yields a negative one.

The electrostatic potential (ESP) maps for PDI2-Pyr4, PDI4-Pyr3 and *P*-PDI8-Pyr7, reveal the pronounced electron-withdrawing character of the oxygen atoms in the imides groups and to a smaller extent this is also present for the Pyr units (Fig. 5.29). Furthermore, the enhanced contrarian electropositive character can be seen in the PDI bay regions.

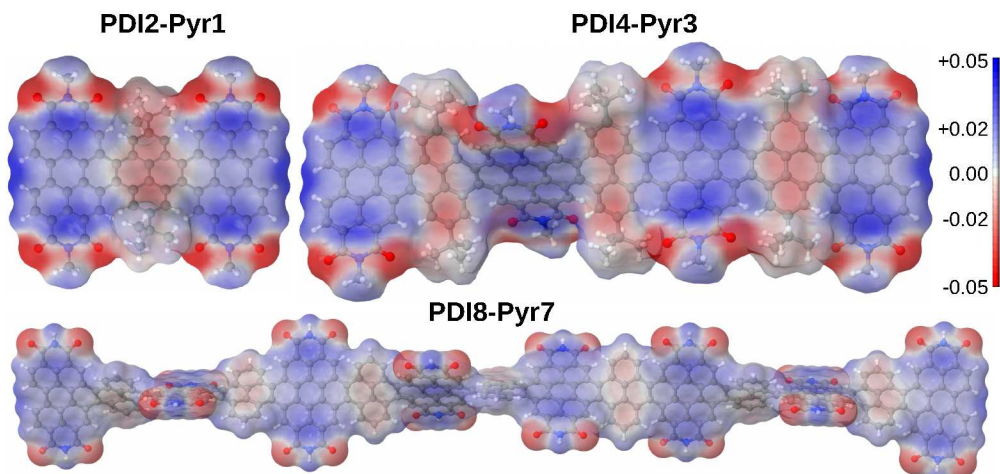


Figure 5.29: ESP maps for PDI2-Pyr4, PDI4-Pyr3 and *P*-PDI8-Pyr7 at the optimised ground state geometry.

The TDDFT absorption spectra of PDI2-Pyr1 and PDI4-Pyr3 resemble the experimental absorption spectra in  $\text{CHCl}_3$  (Fig. 5.30). The TDDFT absorption spectra show a slight red-shift about 15 nm concerning the experimental spectra, which is within the DFT error margin. The spectra for the clockwise rotated *P*-PDI2-Pyr1 and anti-clockwise rotated *M*-PDI2-Pyr1 are identical, whereas the twisted *T*-PDI2-Pyr1 conformation yields a slight red-shift but maintains all main spectral features.

PDI4-Pyr3 exhibits a red-shift in the experimental spectrum of about 36 nm compared to PDI2-Pyr1, e.g. the first absorption band shifts from 578 nm to 614 nm. This trend is also reflected in the TDDFT spectra with a shift from 590 nm to 625 nm. This effect is consistent with the elongation of the conjugated  $\pi$ -system. The helical structures *P*-PDI4-Pyr3 and *M*-PDI4-Pyr3 yield indistinguishable absorption spectra. Moreover, the twisted *T*-PDI4-Pyr3 conformation shows no significant spectral changes.

If the system size is doubled from PDI4-Pyr3 to PDI8-Pyr7, one might expect a further spectral red-shift. However, this is not fulfilled, as the first absorption band is centred at 624 nm for *P*-PDI8-Pyr7, 622 nm for *M*-PDI8-Pyr7 and 620 nm for *T*-PDI8-Pyr7, respectively.

An extension of the chain length leads to an increase in the HOMO energy levels for PDI2-Pyr1 from  $E_{\text{HOMO}} = -5.87 \text{ eV}$  to  $E_{\text{HOMO}} = -5.63 \text{ eV}$  in PDI4-Pyr3. The helical *P*-PDI8-Pyr7 and *M*-PDI8-Pyr7 yield a similar value of  $E_{\text{HOMO}} = -5.67 \text{ eV}$ . The LUMO energies remain at a similar level of  $E_{\text{LUMO}} = -3.19 \text{ eV}$ ,  $-3.17 \text{ eV}$  and  $-3.21 \text{ eV}$ , respectively.

The excitation with the lowest excitation energy in *T*-PDI2-Pyr1 into the  $S_1$  state is a charge-transfer state, as it exhibits a 97.5 % HOMO-LUMO transition with a HOMO localised at the Pyr1 and the LUMO on the two PDI parts (Fig. A.30). The  $S_3$  excitation possesses predominantly  $\pi-\pi^*$ -character due to a significant HOMO-1 to LUMO contribution with 84.4% and a minor HOMO-2 to LUMO+1 transition with 9.6%. The  $S_{12}$  excitation dominates the third absorption band with an 84% HOMO-1 to LUMO+2 contribution.

As *T*-, *P*- and *M*-PDI4-Pyr3 yield similar spectra, we focus in the following on the properties of the *T*-configuration. The charge transfer character of the first excited  $S_1$  state is also found for PDI4-Pyr3, as the attributing HOMO and HOMO-1 are predominantly localised at the Pyr units, and LUMO, LUMO+1, LUMO+2, LUMO+3 are localised at the PDI units (Fig. A.30). One finds an experimental trend for higher molar extinction coefficients in PDI4-Pyr3 than in PDI2-Pyr1 for the first absorption band with  $\varepsilon = 1.93 \times 10^5 \text{ M}^{-1}\text{cm}^{-1}$  at 615 nm in PDI4-Pyr3 compared to  $\varepsilon = 0.38 \times 10^5 \text{ M}^{-1}\text{cm}^{-1}$  at 576 nm in PDI2-Pyr1. This trend is also apparent in the elevated oscillator strength  $f=1.88$  for the  $S_1$  excitation in PDI4-Pyr3 when compared to  $f=0.75$  in PDI2-Pyr1. The experimental central band in PDI4-Pyr3 is assigned to the  $S_{10}$  excitation, which is made up of 87.2% HOMO-4 to LUMO+1 contribution. Furthermore, the elevated absorption for PDI4-Pyr3 yields an outstandingly high molar extinction coefficient  $\varepsilon = 3.38 \times 10^5 \text{ M}^{-1}\text{cm}^{-1}$  at 415 nm. This band can be attributed to a collection of excitations  $S_{29}$ ,  $S_{33}$ ,  $S_{39}$  and  $S_{42}$ , where especially the impact of the  $S_{39}$  excitation is elevated with an oscillator strength  $f=2.78$  for a transition with 45.0% HOMO-3 to LUMO+4 contribution.

The  $S_1$  state in helical *P*-PDI8-Pyr7 possesses a charge-transfer character as HOMO, HOMO-1, HOMO-2 exhibit prevailing contributions on the Pyr units, whereas LUMO+2, LUMO+3, LUMO+4 are localised at the PDI units (Fig. A.32). For instance, the Pyr $\rightarrow$ PDI character is found in the HOMO to LUMO+2 transition, which is the major contributor to the  $S_1$  state with 48.1%. It is also present in the HOMO-1 to LUMO+3 transition with 20.0% contribution. Besides, the  $S_1$  excitation dominates the absorption spectrum as it possesses an outstandingly high oscillator strength  $f=4.56$ . The degenerated states  $S_{21}$  and  $S_{22}$  belong to  $\pi \rightarrow \pi^*$  excitations localised at the PDI terminations of the helical laddered nanoribbon with oscillator strength  $f=0.70$  and  $f=0.74$ , respectively. The third maximum at 480 nm is assigned to the  $S_{37}$  state with  $f=1.05$ .

The helical *M*-PDI8-Pyr7 configuration yields the same spectral features as *P*-PDI8-Pyr7, and one can assign the states  $S_{21}$  and  $S_{22}$  in the *P*-shaped helix to the states  $S_{22}$  and  $S_{23}$  in the helical *M* configuration. All these characteristic spectral features are also present in the spectrum for the twisted structure *T*-PDI8-Pyr7.

The internal reorganization energies for the laddered nanoribbon decreases with expanding molecule size. They yield  $\lambda_h^{\text{in}} = 0.146 \text{ eV}$ ,  $0.102 \text{ eV}$  and  $0.067 \text{ eV}$  for homo-molecular hole transfer in the order PDI2-Pyr1, PDI3-Pyr2 and PDI4-Pyr3 on B3LYP-D3(BJ)/6-31G\* level of theory. In the same manner, one obtains for electron transfer  $\lambda_e^{\text{in}} = 0.161 \text{ eV}$ ,  $0.091 \text{ eV}$  and  $0.069 \text{ eV}$ , respectively. It is a favourable feature for enhanced charge transfer between laddered nanoribbons PDIn-Pyr( $n-1$ ) with increasing length  $n$ .

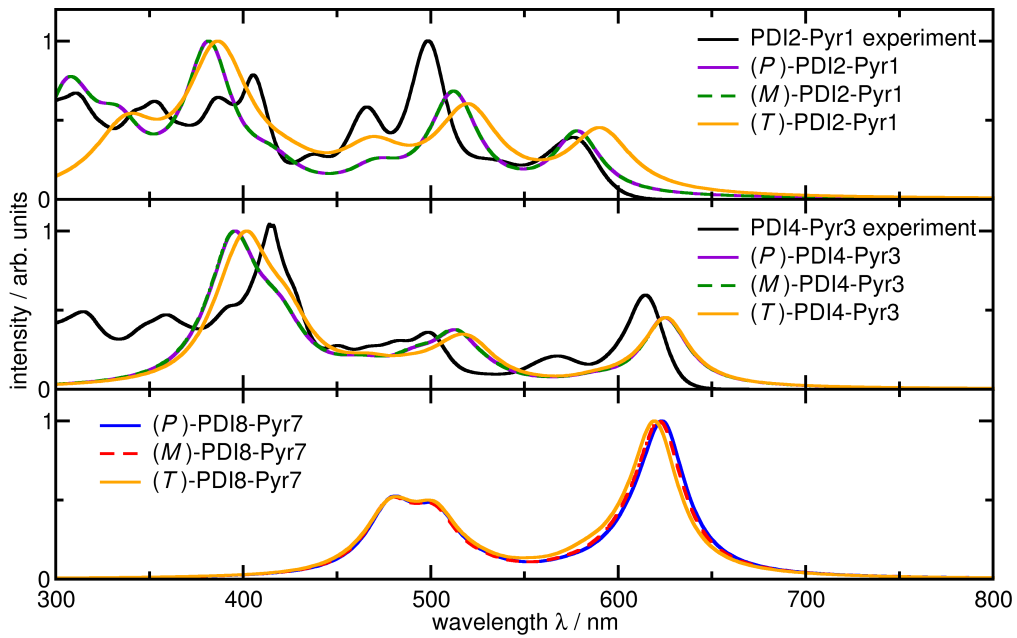


Figure 5.30: Experimental UV-Vis spectra in dilute chloroform solution for PDI2-Pyr1, PDI4-Pyr3 (black). TDDFT absorption spectra CHCl<sub>3</sub> as PCM with Bondi radii on B3LYP-6-31G\* level of theory.

The spectra are displayed for twisted *T*-PDI2-Pyr1 (orange), clockwise rotated *P*-PDI2-Pyr1(violet) and anti-clockwise rotated *M*-PDI2-Pyr1 (green, upper panel).

The helical structures *P*-PDI4-Pyr3 (violet), *M*-PDI4-Pyr3 (green) and twisted *T*-PDI4-Pyr3 (orange, central panel) yield a similar spectral structure.

The TDDFT spectra for the helical structures *P*-PDI8-Pyr7 (blue), *M*-PDI8-Pyr7 (red) and a twisted conformation *T*-PDI8-Pyr7 (orange, lower panel) do not yield a large red-shift with respect to PDI4-Pyr3.

## 5.8 Comparisons of Acceptor Molecules

In the following section, we compare charge transfer properties for acceptor molecules based on optimised ground state S<sub>0</sub> dimer configurations of the same species (homo-molecular pairs). As we do not have access to the orientation of individual molecules inside the BHJ-OSC, we apply the dimer structures as a model for the alignment of molecules inside the amorphous domain. The goal is to identify acceptor molecules with high intra-domain charge transport. Therefore, we compare charge-transfer properties between molecular pairs, e.g. the internal reorganization energies  $\lambda_{AB}^{in}$ , DIPRO-based charge transfer integrals  $|J_{AB}|$  and the Marcus rate expressions  $k_{AB}$  as indicators for hole and electron transport. We remind the reader that  $\Delta E^{in} = 0.0$  eV for homo-molecular charge transfer, and we consider outer-sphere contributions to be small.

**Reorganization Energy** A comparison of the internal reorganization energies  $\lambda_{AB}^{in}$  is depicted in Fig. 5.31 for charge transfer between various homo-molecular pairs of acceptor molecules. The acceptor molecules DIPBI, PPDI, TPH, TPH-Se and cis-PDTI yield higher reorganization energies for hole transfer  $\lambda_h^{in}$  than for electron transfer  $\lambda_e^{in}$ . The opposite holds for PPD, PPD-Se, trans-PDTI and PHHP. All energies are in a similar energetic range between 0.05 eV and 0.20 eV.

DIPBI exhibits the highest  $\lambda_e^{\text{in}} = 0.196$  eV and PPD-Se the lowest 0.081 eV in the selected set of compounds. The highest value  $\lambda_h^{\text{in}} = 0.147$  eV is obtained for PHHP, and the smallest is 0.077 eV for PPDI. The cis-PDTTI has a lower  $\lambda_h^{\text{in}}$  than  $\lambda_e^{\text{in}}$ , whereas in trans-PDTTI the role is reversed. The selenium-annulation only has a minor, rising influence on the reorganization energies, except for electron transfer between PPD-Se. The three-bladed TPH and TPH-Se exhibit higher reorganization energies than the five-bladed PPD and PPD-Se. This finding is in line with the general trend for a reduction in  $\lambda^{\text{in}}$  with increasing system size in both in acceptor molecules, e.g. PDIn-Pyr( $n - 1$ ) (Sec. 5.7) and in donor polymers [282], e.g. in P3MT (Fig. 3.25) and PBDT-TS1 (Fig. 4.39).

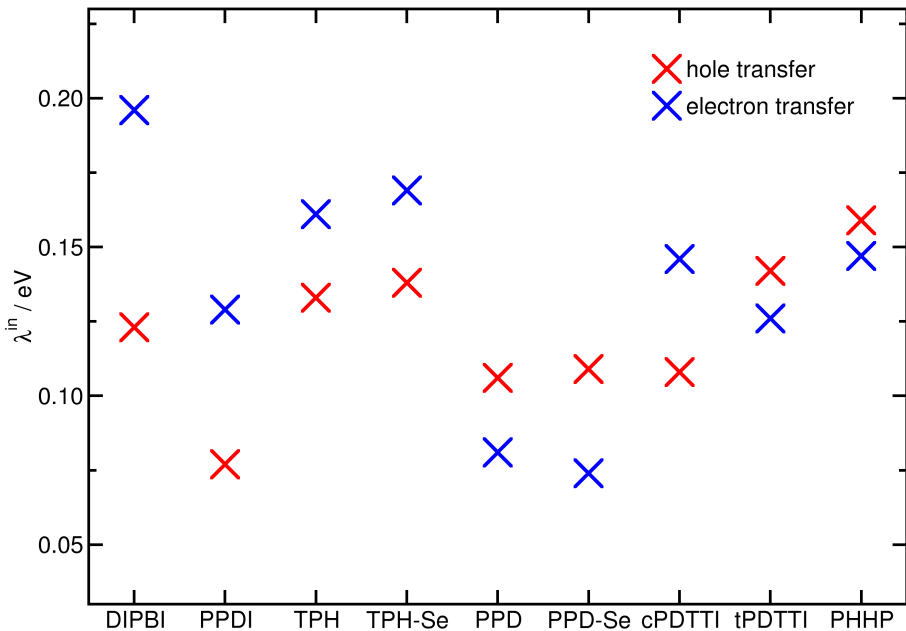


Figure 5.31: Internal reorganization energy for hole  $\lambda_h^{\text{in}}$  and electron transfer  $\lambda_e^{\text{in}}$  using B3LYP-D3(BJ)/6-31G\* on vacuum level. The acceptor molecules are DIPBI, PPDI, TPH, TPH-Se, PPD, PPD-Se, cis-PDTTI, trans-PDTTI and PHHP.

Reorganization energies  $\lambda_h^{\text{in}}$  and  $\lambda_e^{\text{in}}$  on PBE0-D3(BJ)/6-31G\* level of theory yield the same trends but are about 0.01 eV lower in energy than the corresponding B3LYP data. The functional dependence of the reorganization energy is well known and it is found that pure functionals underestimate  $\lambda^{\text{in}}$  values obtained by an empirical IP-tuning technique [423]. However, pure DFT is capable of predicting correct trends for different compounds [423,424].

**Charge Transfer Integral** We concentrate on DIPRO-based charge transfer integrals for optimised ground state dimer configurations. The averages for  $|J_{AB}|$  are basically at the same order of magnitude. DIPBI, PPDI, TPH, TPH-Se, cis-PDTTI, trans-PDTTI and PHHP yield higher  $|J_{AB}^h|$  for hole transfer than for electron transfer  $|J_{AB}^e|$  (Fig. 5.32). PPD and PPD-Se are an exception. For them, the order is reversed, and both provide low values for  $|J_{AB}^h| \approx 1$  meV. The largest  $|J_{AB}^h| = 0.098$  eV and  $|J_{AB}^e| = 0.068$  eV are found for the trans-PDTTI dimers. They arise due to the pronounced intermolecular interaction in the  $\pi$ -stacks with a co-facial packing for both PDI-subunits. PHHP exhibits the smallest  $|J_{AB}^e| = 7.6$  meV.

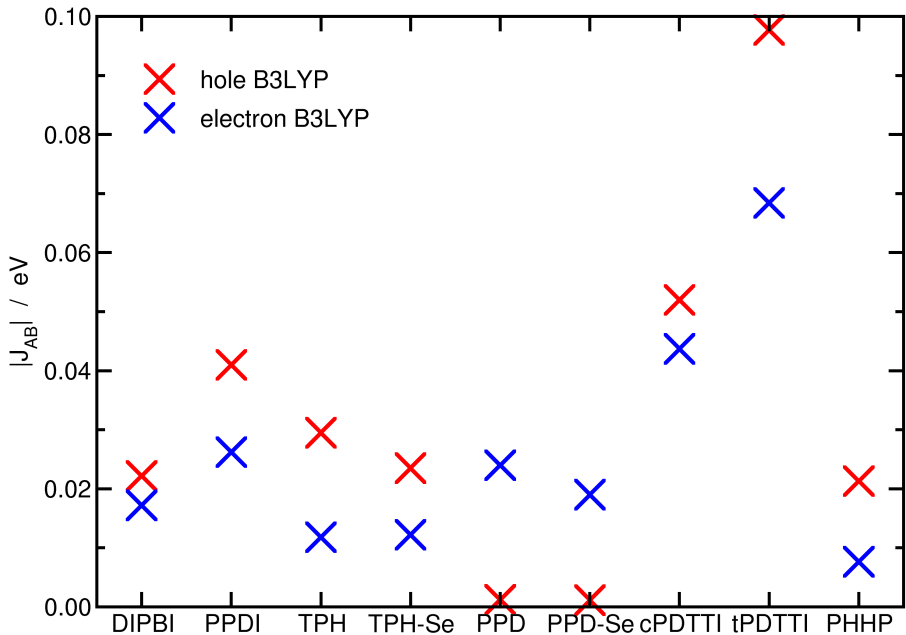


Figure 5.32: Average DIPRO charge transfer integral for hole  $|J_{AB}^h|$  and electron transfer  $|J_{AB}^e|$  B3LYP-D3(BJ)/6-31G\* on vacuum level. The acceptor molecules are DIPBI, PPDI, TPH, TPH-Se, PPD, PPD-Se, cis-PDTI, trans-PDTI and PHHP. We average  $|J_{AB}|$  for six DFT-optimised dimer configurations for each molecular species.

**Marcus Rates** The averaged charge transfer rates can vary about four orders of magnitude between  $10^{11} \text{ s}^{-1}$  and  $10^{15} \text{ s}^{-1}$ , when comparing the different acceptor molecules (Fig. 5.33). In general, the electron transfer rates  $k_{AB}^e$  are higher than the corresponding rates  $k_{AB}^h$  for holes. The order is reversed only for TPH, where the rates only differ by about a factor of 2. The electron transfer rates are significantly higher than the hole transfer rates in all three compounds TPH-Se, PPD and PPD-Se. Mainly, the comparatively lower  $|J_{AB}^h|$  causes this finding in PPD and PPD-Se. PDTI yields the highest  $k_{AB}^e = 2.13 \times 10^{14} \text{ s}^{-1}$  in the trans-PDTI conformation and a remarkable value  $k_{AB}^e = 7.13 \times 10^{13} \text{ s}^{-1}$  for cis-PDTI. This property is attributed to both beneficial, high  $|J_{AB}|$  and moderate  $\lambda^{\text{in}}$ .

Our investigated charge transfer properties detail that cis-PDTI and especially trans-PDTI are promising candidates for electron transport in organic semiconductors. They yield the best performance in the set of selected acceptor molecules. As experimental techniques do not give access to  $\lambda^{\text{in}}$ ,  $|J_{AB}|$ , and  $k_{AB}$  of individual molecular pairs, we compare the results to the power conversion efficiency (PCE) in OSC devices, (which is obtained in combination with an adjusted donor polymer).

An encouraging trend is that the average charge transfer rates  $k_{AB}^{h,e}$  for PPDI dimers are superior to those for DIPBI dimers, which coincides the experimental findings of higher the PCE of about 5.4% in PBDT-RS1:PPDI [311] compared to 3.63% in P3HT:DIPBI [63]. However, one does not find significantly enhanced transfer rates for TPH and TPH-Se, which give rise to a higher PCE of about 9.25% in PDBT-TS:TPH-Se [320]. It stands to reason that the latter improvement is not driven by unique properties at the molecular level, but mainly by the improved connectivity of the conductive regimes inside the morphology. Hence, the tendencies in  $k_{AB}$  cannot reflect the general trend of the PCE in OSCs.

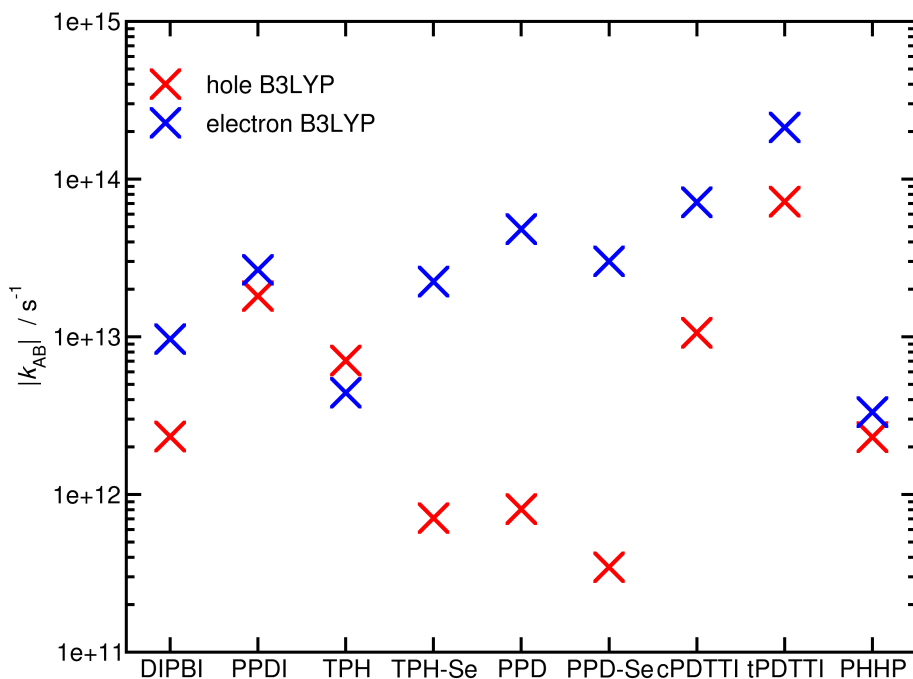


Figure 5.33: Averaged Marcus charge transfer rates for hole  $k_{AB}^h$  and electron transfer  $k_{AB}^e$  on B3LYP-D3(BJ)/6-31G\* level. The acceptor molecules are DIPBI, PPDI, TPH, TPH-Se, PPD, PPD-Se, cis-PDTI, trans-PDTI and PHHP. We average  $k_{AB}$  for six DFT-optimised dimer configuration. The external field  $|\mathbf{F}^{\text{ext}}| = 1 \times 10^7 \text{ V m}^{-1}$  is oriented parallel to the COM connecting vector  $\mathbf{d}_{\text{COM}}$  of both dimers. Outer-sphere contributions are neglected.

The influence of the total three-dimensional morphology on charge transport can only be approximated by a selected set of dimers. Not only energetically favourable dimer configurations are present in the blend morphology. Consequently, the selected sets of dimers represent only a limited outtake of possible arrangements, and even though the total energy of a given dimer configuration is high, the charge transfer properties are not reduced necessarily. This study shows that apart from  $\pi$ -stacking motives also dimer aggregation patterns including lateral-shifted stacks or T-stacks can have a high impact on charge transfer. Particularly, the latter can exhibit moderate  $|J_{AB}|$  and hence result in remarkable  $k_{AB}$ . One should bear in mind that outer-sphere contributions are neglected within these calculations, which can also influence the role of charge transfer donor and acceptor, especially at the donor-acceptor interface [31, 224].

All in all, looking only at charge transfer properties of individual components is not sufficient to understand the overall performance of organic solar cell devices. The presented results yield interesting trends, even though dynamical fluctuations of site-energies and electronic couplings are not included in the model. That is why we need a multiscale approach to model the physical processes and get a decent description of the underlying morphology.

